JGR Oceans

RESEARCH ARTICLE
10.1029/2023JC020107

Structure and Variability of Iceland Scotland Overflow Water Transport in the Western Iceland Basin

M. Devana[1] and W. Johns[1]

[1]Rosenstiel School of Marine, Atmospheric, and Earth Sciences, University of Miami, Coral Gables, FL, USA

Key Points:

- Iceland Scotland Overflow transport variability is governed by a combination of barotropic and topographic effects
- Transport variability along the Reykjanes Ridge slope is dominated by deep ageostrophic flow within an axial rift valley
- Ageostrophic transport accounts for ~30% of Iceland Scotland Overflow Water (ISOW) transport along the Reykjanes Ridge flank and is a significant component of net ISOW export

Supporting Information:

Supporting Information may be found in the online version of this article.

Correspondence to:

M. Devana,
devanamarsci@gmail.com

Citation:

Devana, M., & Johns, W. (2024). Structure and variability of Iceland Scotland Overflow Water transport in the Western Iceland Basin. *Journal of Geophysical Research: Oceans*, *129*, e2023JC020107. https://doi.org/10.1029/2023JC020107

Received 5 JUN 2023
Accepted 2 JUL 2024

Author Contributions:

Conceptualization: M. Devana, W. Johns
Data curation: M. Devana
Formal analysis: M. Devana, W. Johns
Funding acquisition: W. Johns
Investigation: M. Devana
Methodology: M. Devana, W. Johns
Project administration: W. Johns
Software: M. Devana
Supervision: W. Johns
Validation: M. Devana
Visualization: M. Devana
Writing – original draft: M. Devana
Writing – review & editing: M. Devana, W. Johns

Abstract The Iceland Scotland Overflow Water (ISOW) plume supplies approximately a third of the production of North Atlantic Deep Water and is a key component of the meridional overturning circulation (MOC). The Overturning in the Subpolar North Atlantic Program (OSNAP) mooring array in the Iceland Basin has provided high-resolution observations of ISOW from 2014 to 2020. The ISOW plume forms a deep western boundary current along the eastern flank of Reykjanes Ridge, and its total transport varies by greater than a factor of two on intra-seasonal timescales. EOF analysis of moored current meter records reveal two dominant modes of velocity variance. The first mode explains roughly 20% of the variance and shows a bottom intensified structure concentrated in the rift valley that runs parallel to the ridge axis. The transport anomaly reconstructed from the first mode explains nearly 80% of the total ISOW plume transport variance. The second mode accounts for 15% of velocity variance, but only 5% of the transport variance. The geostrophically estimated transport (2.9 Sv) recovers only 70% of the total ISOW transport along the ridge flank estimated from the direct current meter observations (4.2 Sv), implying a significant ageostrophic component of ISOW mean transport and variability. Ageostrophic flow is strongly linked to the leading mode of velocity variability within the rift valley. The ISOW transport variability along the upper and middle part of the ridge is further shown to correlate with changes in the strength of deep MOC limb across the basin-wide OSNAP array.

Plain Language Summary The Iceland Scotland Overflow (ISOW) as a major component of deep ocean circulation in the North Atlantic. Newly available mooring observations from the Overturning in the Subpolar North Atlantic Program show that this current has significant intra-seasonal variability. This study shows that the flow is strongly affected by the topography of the Reykjanes Ridge which splits the current into multiple branches on the ridge slope and in the Iceland Basin interior. Most of the ISOW transport occurs along the ridge while the basin interior flow dominates the net variability. The results show that a major portion of the flow variability along the ridge is driven by flow funneled through a rift valley along the ridge slope. Geostrophic estimates of transport (the classic method of estimating large scale transport in the ocean) in this region fail to recover the flow within the rift valley.

1. Introduction

Iceland Scotland Overflow Water (ISOW) is formed by cold, dense Nordic Sea waters that spill over the Iceland-Scotland Ridge into the Iceland Basin primarily as a gravity current through Faroe Bank Channel. As the waters descend into the Iceland Basin, ambient mid-depth waters are entrained into the overflow plume, comprised mainly of Subpolar Mode Water and Labrador Sea Water (Beaird et al., 2013; Hansen & Østerhus, 2000; Johns et al., 2021). After descending into the basin, ISOW adjusts to form a topographically steered boundary current flowing westward along the Iceland Faroe Ridge which then turns southward along the Reykjanes Ridge. The ISOW layer is identified by waters with potential densities greater than 27.8 kg/m^3 and exhibits a characteristic bottom enhanced salinity signal from the entrained Subpolar Mode Waters. After circulating along the western perimeter of the Iceland Basin, ISOW is exported into the western North Atlantic through fracture zones in the ridge and to the eastern North Atlantic (Bower et al., 2009; Hansen & Østerhus, 2000; W. Johns et al., 2021; Petit et al., 2020). It combines with Denmark Strait Overflow to form Lower North Atlantic Deep Water that flows southward as the dominant water mass of the Atlantic Meridional Overturning Circulation (AMOC)'s lower limb.

Considerable research over the past few decades has focused on examining the ISOW pathways and formation mechanisms, how ISOW is exported into various regions of the Atlantic, what sets its water mass properties, and how it contributes to overturning circulation in the Subpolar Gyre (Beaird et al., 2013; Devana et al., 2021; Johns

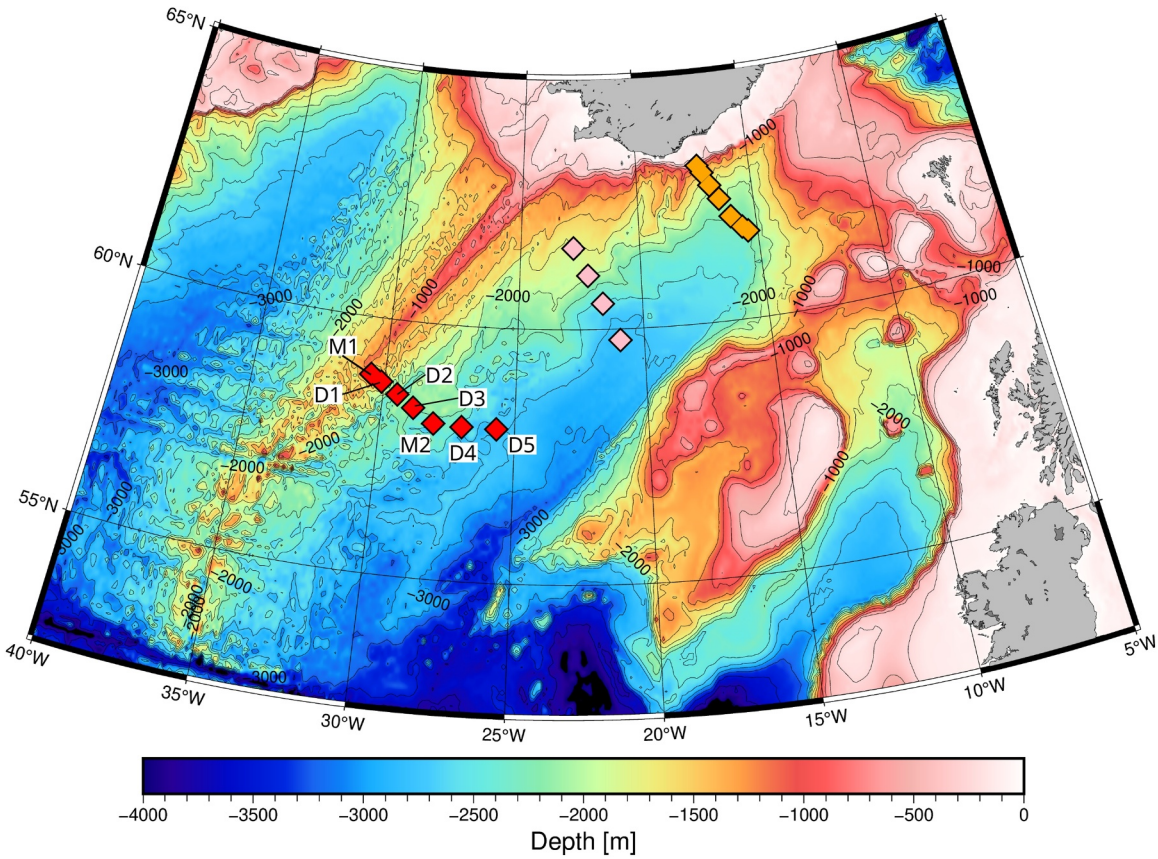

Figure 1. Bathymetry of Iceland Basin from the GEBCO global data set with 250-m interval contours. The location of the OSNAP (red), Kanzow and Zenk (2014) (pink) and Saunders (1996) (orange) moorings are indicated with red, pink, and orange squares, respectively. OSNAP mooring locations are labeled with individual mooring names.

et al., 2021; Kanzow & Zenk, 2014; Lozier et al., 2019, 2022; Saunders, 1996; Xu et al., 2018; Zou et al., 2017). However, despite ISOW's key role in the AMOC, our understanding of its transport variability is limited. Now, using observations from the recent Overturning in the Subpolar North Atlantic Program (OSNAP) mooring array (Lozier et al., 2019), we can gain new insight into the highly variable ISOW export from the Iceland Basin and how that affects the basin-wide overturning circulation.

ISOW transport variability was previously examined by two mooring arrays upstream of the OSNAP line, deployed by Saunders (1996) and Kanzow and Zenk (2014), and is currently monitored by the OSNAP mooring array. We present results from 6 years of OSNAP mooring observations (2014–2020). The locations of each of these arrays are shown in Figure 1. The first moored array was deployed by Saunders (1996) who estimated a mean ISOW transport of 3.2 Sv along the southern Icelandic slope. His results show key aspects of the overall structure and variability of the ISOW plume and highlighted the presence of intra-seasonal variability. At this array, there is a singular core of relatively steady, along-isobath flow along the slope and substantial intra-seasonal variability in deeper waters toward the interior of the Iceland Basin. Saunders hypothesized that much of the variability on weekly to monthly timescales was due to baroclinic instability within the ISOW layer but he was unable to verify or test this idea. Kanzow and Zenk (2014) provided an updated estimate of ISOW with a mooring array deployed farther downstream that showed a mean transport of 3.8 Sv. Their results also showed a similar structure: a dominant core of flow oriented along the topography and variable cross-slope flow farther down the slope. They proposed that Topographic Rossby Waves could explain much of the intra-seasonal variability. However, their mooring array lost its western-most mooring near the ridge crest and velocities there were estimated by mean values derived from RAFOS floats. As a result, their description of total ISOW variability may be missing aspects of flow structure and variability associated with flow along the ridge crest. Neither array was deployed for long enough to clearly assess interannual or long-term trends.

The latest, and ongoing, mooring deployment in the region is the OSNAP array which is placed farther south along the Reykjanes Ridge near 58°N (Figure 1). This mooring array is more extensive in spatial coverage and provides higher resolution with more instruments than either the Saunders (1996) or Kanzow and Zenk (2014) ISOW arrays and is the longest continuous record of ISOW (2014–2020 July) to date. The first observations reported from the OSNAP array displayed considerable variability of ISOW transport over a range from 15 Sv to −5 Sv (positive southward indicating export from the basin) (Johns et al., 2021). The magnitude of the variability is surprising since flow at Faroe Bank Channel is known to be far more stable (Hansen et al., 2016; Hansen & Østerhus, 2000, 2007). In this study we provide a comprehensive analysis of ISOW transport variability, compare results with previous observational and model-based studies, identify key modes of flow variability, and show that a significant portion of the flow may be governed by ageostrophic dynamics.

2. Materials and Methods

The principal data used for this study are the 6-year (July 2014–August 2020) time series of moored velocity, temperature, and salinity measurements from the OSNAP array. We focus on the OSNAP section extending from the Reykjanes Ridge crest eastwards to the interior of the Iceland Basin (moorings M1 to D5; Figure 1). These records are combined to produce a daily, 40-hr low passed gridded data set of all observed parameters following the procedure applied in Johns et al. (2021) but extended by an additional two years to include the 2018–2020 observations. The configuration of the instruments is shown in Figure 2 and further details can be found in Johns et al. (2021). Moorings M1, and M2 are full water column "dynamic height" moorings while D1, D2, D3, D4, and D5 are short moorings with instruments focused on resolving the ISOW layer. All the instrument levels below 1,200 m are paired with T/S and current meters for concurrent measurements. For the remainder of this manuscript we consider the flow in a rotated frame where the alongslope flow (parallel to the ridge axis) is along 215°T (True North) and the cross-slope flow is along 125°T. The transport calculations utilize the along slope component across the OSNAP array such that positive transports correspond to southward export of ISOW from the Iceland Basin.

The observations from the mooring array are combined to generate gridded, time-evolving fields that can be integrated in the vertical and cross slope directions to calculate along slope transport. Due to the Reykjanes Ridge bottom slope and complex topography, "bottom triangles" are created, where lateral gradients are not directly resolved and must be therefore be filled using interpolation methods. Here we apply commonly used methods used for filling bottom triangles in hydrographic sections (Ganachaud, 2003). First, at each mooring vertical shape-preserving splines are constructed at each timestep from 1,200 m to the bottom. A 40 hr lowpass filter is applied to each instrument record prior to construction of the vertical splines. To fill in the bottom triangles between moorings, the splined velocity profiles are extrapolated downwards using observations from the neighboring deeper mooring profiles. For the gridded fields shown here and in Johns et al. (2021), the deepest instrument measurements from the adjacent (deeper) mooring were appended to the shallower (upslope) mooring and vertically interpolated to fill the vertical profile (e.g., for mooring D1 the deepest measurement level on D2 (2,420 m) was inserted below the topography at the location of mooring D1 and a shape-preserving spline was used to interpolate the vertical profiles at D1; similarly for mooring D3 using the deepest measurement level from D4, etc.). Further details of the gridding process may be found in Johns et al. (2021). Other methods of vertical profile extension, including linear and cubic spline extrapolation from the deepest measurement levels on each mooring with a constant vertical gradients were tested with no significant change to the results (Text S2 in Supporting Information S1).

Next, the vertical spline profiles are used to generate a 2-D gridded field at each timestep using the MATLAB triangulation-based "natural neighbor" interpolation method which is subsequently masked using high resolution topography along the OSNAP mooring line and daily averaged. The resulting daily gridded fields of temperature, salinity, and along slope flow (positive southwestwards) span from the ridge crest eastwards to mooring D5 from 1,200 m to the seafloor (Figure 2). Daily gridded potential density (σ_θ) fields are calculated using the temperature and salinity fields with the TEOS-10 seawater toolbox. The transport estimates of ISOW presented throughout this manuscript are calculated by integrating the gridded alongslope velocity field from the 27.8 kg/m^3 potential density isopycnal to the seafloor. In Section 3.5, we also utilize the gridded temperature and salinity fields to calculate the thermal wind shear across the ridge slope to estimate the geostrophic velocity field and associated transports. The thermal wind shear is referenced to the 1,200 m level velocities (where current meter observations are present at each mooring) to obtain absolute geostrophic velocity fields which can be used to calculate

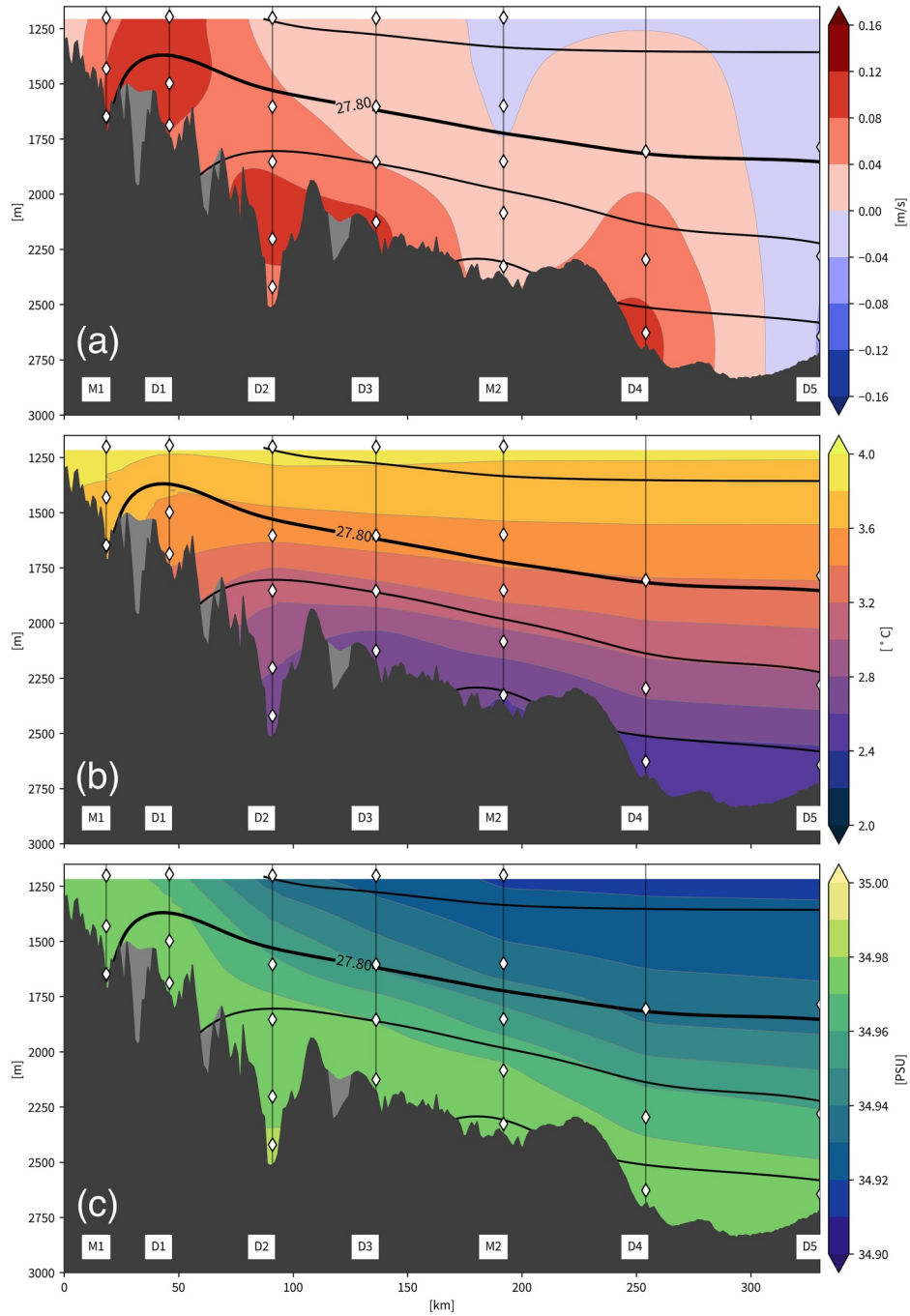

Figure 2. Gridded, time mean along slope velocity, temperature, and salinity (top to bottom) from the OSNAP mooring observations spanning 2014 July to 2020 July. X-direction is along slope distance from the ridge axis in kilometers along the OSNAP line (positive eastwards). Black vertical lines and diamonds indication mooring and instrument locations, respectively. Data gridding was done following the procedure described in Johns et al. (2021). Black solid contours indicate potential density isopycnals at 0.05 kg/m^3 intervals. The labeled 27.8 kg/m^3 isopycnal denotes the ISOW layer. Gray shaded regions of topography indicate topographic masking.

transport. Given the horizontal resolution of the mooring array and the complex topography of the Reykjanes Ridge, uncertainty arises in thermal shear estimated from the gridded products, particularly within the rift valley where mooring D2 is located. The implications are explored in further detail in Section 3.5 and the reader is also referred to Text S2 and S3 in Supporting Information S1 for further validation of the gridding methods.

The observations are supplemented with altimetry measurements over the observational period of the moorings to estimate surface geostrophic velocities in the Iceland Basin (Aviso + Altimetry analysis, obtained from Copernicus Marine Environmental Monitoring Service (CMEMS)). Geostrophic velocities are used to investigate the upper ocean influences on ISOW layer flow. Finally, we include estimates of the Meridional Overturning Circulation (MOC) from 2014 to 2020 across the entire OSNAP-East array from Scotland to Greenland (Fu et al. (2023a)) for comparison with our estimates of ISOW transport within the Iceland Basin.

3. Results

3.1. Mean Structure of the ISOW Layer

The time-mean structure of the ISOW flow at the OSNAP array (Figure 2) shows three cores of southward flow along the Reykjanes Ridge flank centered around moorings D1, D2, and D4, consistent with the first 4 years of observations described by Johns et al. (2021). A northward flow is typically found east of the ridge slope in the Iceland Basin interior at mooring D5. The flows at D2 and D4 are variable in strength but do not show significant meandering zonally across the OSNAP line, due largely to topographic constraints. Mooring D2 is located within a deep rift valley extending 200 km upstream from the mooring array that appears to channel a portion of the ISOW flow and trap it from meandering zonally along the ridge slope. At mooring D4 the flow is banked against the edge of a major topographic feature that extends back northwards along the deep ridge flank several hundred kilometers upstream (Figure 1). This topographic feature, which also contains a sill marking the northern end of the D2 rift valley, is believed to split the single ISOW core observed farther upstream by both Kanzow and Zenk (2014) and Saunders (1996) (see Johns et al., 2021). Model simulations and the presence of major sediment drifts in the basin also show that significant branching of the flow occurs as the topography transitions from the smooth Icelandic slope to the rough Reykjanes Ridge (Johns et al., 2021; Xu et al., 2018; Zou et al., 2017). The flow at mooring D1, which only encounters smaller scale topography along the upper ridge slope, exhibits some cross ridge meandering unlike the flow at D2 and D4. Additionally, the D1 velocity core is not confined solely to the ISOW layer. Here the bottom intensified flow extends upward into the East Reykjanes Ridge Current (ERRC) that transports Icelandic Slope Water and Modified Subpolar Mode Water southward along the ridge crest above the ISOW layer (Johns et al., 2021; Koman et al., 2022). Note that while the flow is divided into distinct cores, temperature and salinity are more uniformly distributed across the ISOW layer (Figures 2b and 2c). Temperature decreases consistently with depth and is the dominant control on the stratification in the layer, while salinity displays the characteristic bottom-enhancement (increasing salinity with depth) derived from entrainment of Subpolar Mode Water.

3.2. ISOW Transport and Variability

The mean transport estimated from the daily averaged, 40-hr low passed observations is 5.8 Sv (positive southward) with a standard deviation of 3.4 Sv, a slight increase from the 2014–2018 estimate of 5.3 Sv mean transport reported by Johns et al. (2021). The total transport exhibits significant variability on intra-annual timescales with daily transports ranging from nearly 15 Sv southwards to periods of net northward flow (Figure 3a). No significant seasonal cycle is observed, unlike observations at Faroe Bank Channel where the overflow exhibits seasonality driven by barotropic modulation (Lake & Lundberg, 2006). Similarly, no seasonal cycle is evident at either the Saunders (1996) or Kanzow and Zenk (2014) mooring arrays, suggesting that by the time the ISOW flow reaches these mooring arrays the seasonal cycle at FBC has been erased or masked by other variability.

To better understand the transport variability, we split the transport integration into two sectors: the region between moorings M1 to M2 along the upper ridge slope (ISOW-West), and the region between moorings M2 to D5 on the lower ridge slope (ISOW-East). The ISOW-West sector contains the two cores of ISOW flow along the upper and mid-ridge slope, around moorings D1 and D2, while ISOW-East includes the off-ridge deep core flowing at the base of the ridge topography near mooring D4 and the northward flow at D5. Transport across these two sectors is not significantly correlated during the observation period, suggesting the presence of dynamically distinct regions of flow. The majority of the ISOW plume transport is carried in the ISOW-West sector (4.4 Sv, or about 75% of the total transport), while the remainder (1.4 Sv net southward transport) occurs in the ISOW-East sector. However, ISOW-East dominates the variability of the total transport, with ISOW-West showing substantially less variability than the eastern portion of flow at nearly all timescales (Figures 3 and 4). Both ISOW

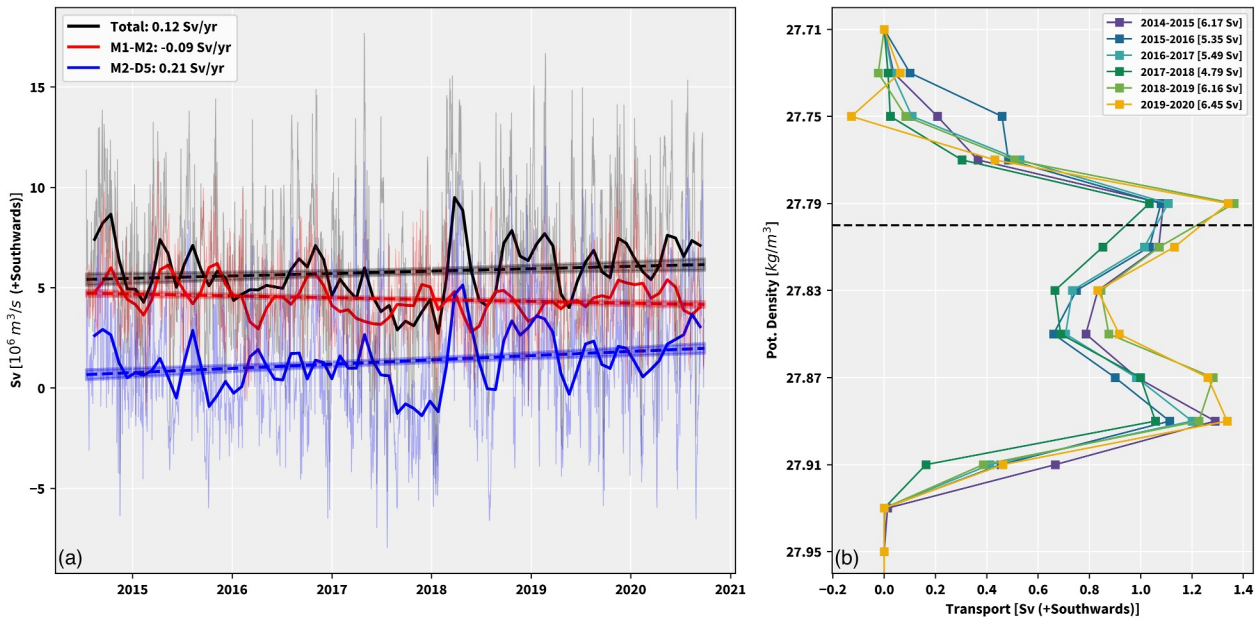

Figure 3. (a) ISOW 60 days low passed, monthly averaged transport (bold) and daily averaged (thin lines), positive southwards, across the OSNAP array. Total (black), Eastern (red), and Western (blue) transports are shown to demonstrate the partitioning of transport and variability along the ridge slope versus the interior Iceland basin. The averaging applied is for allowing comparison to Kanzow and Zenk (2014). Shading indicates 95% confidence intervals of linear regressions. (b) Yearly averaged ISOW transport in 0.02 kg/m^3 potential density bins. Note that the density range extends above the ISOW layer into the base of East Reykjanes Ridge Current.

East and West are dominated by intra-seasonal variability and have substantially weaker inter-annual variability. The periods of net northward transport across the OSNAP array appear to be largely driven by strong northward flow events across ISOW-East that cancel out the nearly always southward flow in the ISOW cores along the middle and upper ridge.

Over the 6-year mooring record we observed a weakly increasing trend of 0.12 Sv/year ($p < 0.05$). The trends in the two section's transport are opposing, with an increase in ISOW-East, 0.21 Sv/year ($p < 0.05$), and a slightly weaker decrease in ISOW-West, −0.09 Sv/year ($p < 0.05$). The net effect is a weakly increasing trend in overall

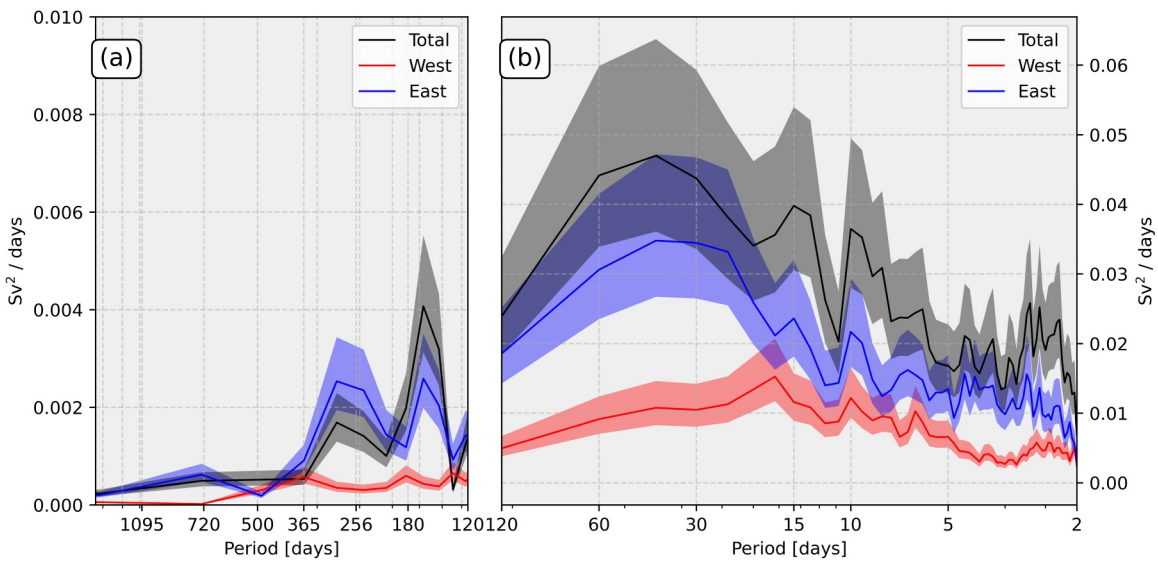

Figure 4. Transport variance preserving spectra calculated using 4-year (a) and 120 days (b) half overlapping windows with Welch's method for Total, ISOW-West, and ISOW-East daily averaged transport time series, with the *x*-axis indicating period in days and shading indicates 95% confidence interval. Separate windows are used to examine low and high frequency variability more clearly. Note that the two panels have different y scales.

transport. The increasing transport (increasing southward export) in ISOW-East is largely attributed to strengthening flow in the D4 branch of flow at the base of the ridge slope where southward flow at the bottom current meter of D4 saw a sustained increase from 5 to 6 cm/s in 2014–2015 to 8–10 cm/s in 2019–2020 (annual averages are taken over period spanning July 1st through June of the following year). It is unclear what has driven this increase in deep flow at D4, but the results suggest that a larger portion of the ISOW plume may have been diverted eastward around the upstream topographic feature noted previously, to flow along the deeper plume pathway near D4. The observed trends are weak compared to the intra-seasonal variability of the plume branches, especially for the deep plume branch, and therefore these trends could also result from inherent variability of the ISOW flow rather than indicating a meaningful shift in ISOW pathways.

We also examine the ISOW transport in density space to show that transport is bimodally distributed through the ISOW density ranges. Figure 3b shows that transport is largely partitioned between a lighter core that also includes lower ERRC waters and a denser core deeper in the ISOW layer (Koman et al., 2022). The lighter core corresponds to the flow seen near the ridge crest near moorings M1 and D1 in Figure 2a while the deeper core corresponds to the flow within the rift valley at D2 and at the base of the ridge where D4 is located. The weaker transport in intermediate density ranges (σ_θ = 27.82–27.86 kg/m^3) is due to the relative flow minimum in this density range between the upper branch of flow near mooring D1 and the strongly bottom intensified flow farther down the ridge slope (Figure 2). The partitioning into two density classes within ISOW may also be a consequence of upstream branching that causes the densest waters to descend along the ridge slope while lighter waters stay high on the slope and mix with the deep portion of the ERRC. The general partitioning of transport remains consistent through all years of the observations, but magnitudes show considerable interannual variability through the entire layer. Transport was at a minimum through the entire density range in 2017–2018 which appears to be almost entirely driven by a substantial decrease in ISOW-East transport. In the following year (2018–2019), transport increases to a maximum through the entire layer, also driven by a large increase in ISOW-East which saw a major spike in transport reaching nearly 5 Sv (nearly 10 Sv across the whole array). ISOW transport is also clearly linked with the near-bottom flow of the ERRC and raises a question of whether the 27.8 kg/m^3 potential density surface that is typically used as an upper limit for the ISOW layer is really an appropriate threshold for ISOW.

As shown in Johns et al. (2021), the deepest waters of the ERRC (σ_θ = 27.71–27.8 kg/m^3) contain small amounts of Norwegian Sea Overflow waters that are mixed with Subpolar Mode Waters to form Icelandic Slope water. Figure 3b shows that substantial transport occurs around σ_θ = 27.79 kg/m^3, just above the 27.8 kg/m^3 threshold that is historically used to indicate the ISOW layer. Therefore, to fully account for all of the original Norwegian Sea Overflow waters that contribute to the lower limb of the AMOC, a more detailed water mass analysis is necessary. However, since the bulk of the Norwegian Sea overflow contribution is below σ_θ = 27.8 kg/m^3, we will continue to use the traditional definition of ISOW as the transport occurring at $\sigma_\theta \geq$ 27.8 kg/m^3 for consistency with historical references.

We compare the transport variability at the OSNAP array with estimates from the two previous ISOW arrays deployed by Kanzow and Zenk (2014) and Saunders (1996) to examine how the ISOW transport variability evolves along its downstream path (Table 1). Table 1 shows the mean and standard deviation estimates of transport for the total, east, and west branches of ISOW from the OSNAP array's daily estimates, as well as from 5-day and 60-day averages that can be compared directly with the values quoted by Saunders (1996) and Kanzow and Zenk (2014), respectively. We also compare with transport variability estimates from the model results shown by Xu et al. (2018) and Zou et al. (2017) near the OSNAP line. Saunders (1996) shows a standard deviation of 1.4 Sv from their 5-day averaged estimates which is approximately half of the comparable 5-day averaged OSNAP estimates. However, the variability of the OSNAP-West transport along the upper ridge flank (1.56 Sv) is comparable to that observed by Saunders, indicating that most of this increase in variance between the two arrays is due to the large variability of the deeper OSNAP-East plume branch. Kanzow and Zenk (2014) do not provide variance estimates on daily or 5-day time scales, but the standard deviation of their 60-day averaged estimates (1.35 Sv) is very similar to that observed at the OSNAP array (1.42 Sv). This suggests that the low-frequency variability of the ISOW plume is already well established by the time it has traveled the ∼300 km from the Saunders to Kanzow and Zenk arrays. Estimates from the model-based studies by Zou et al. (2017) and Xu et al. (2018) both show weak transport variability that is notably less than any of the observational estimates. At the OSNAP line the standard deviations of the model transports are 5–6 times smaller than the observations,

Table 1
Comparisons of ISOW Transports From This Study With Previous Observational and Model-Based Studies

Study	Mean transport (Sv)	Daily std.	5-Day average std.	60-day average std.
OSNAP Total	5.78	3.54	3.03	1.42
ISOW-West	4.44	1.85	1.56	0.78
ISOW-East	1.33	3.07	2.70	1.37
Saunders (1996)	3.2	–	1.4	-
Kanzow and Zenk (2014)	3.80	–	–	1.35
Xu et al. (2018)	**3.02 (0.55 std)**	–	–	–
Zou et al. (2017)	**3.8 (0.7 Sv)**	–	–	–

Note. Transports are given in Sv (10^6 m^3/s). The first column indicates mean transport, and the remaining columns show standard deviation at different averaging levels. Bold transport values from Xu et al. (2018) and Zou et al. (2017) are given by the authors without further information on any temporal averaging or filtering.

clearly indicating that the model representations of the ISOW plume are too stable and that the models may be missing key dynamics associated with the ISOW plume variability.

Variance ellipses of subinertial flow from current meters at the bottom 3 instrument levels of each mooring show that the time mean flow (2014 July to 2020 July) orientation and vertical structure of variance in the bottom layer varies significantly across the array (Figure 5). A 40 hr lowpass filter is applied to remove tidal influences prior to calculation of spectra. At M1 the near bottom flow is strongly directional with a noticeable down-slope component. The flow becomes weaker and more isotropic farther up in the water column. At D1 there is a

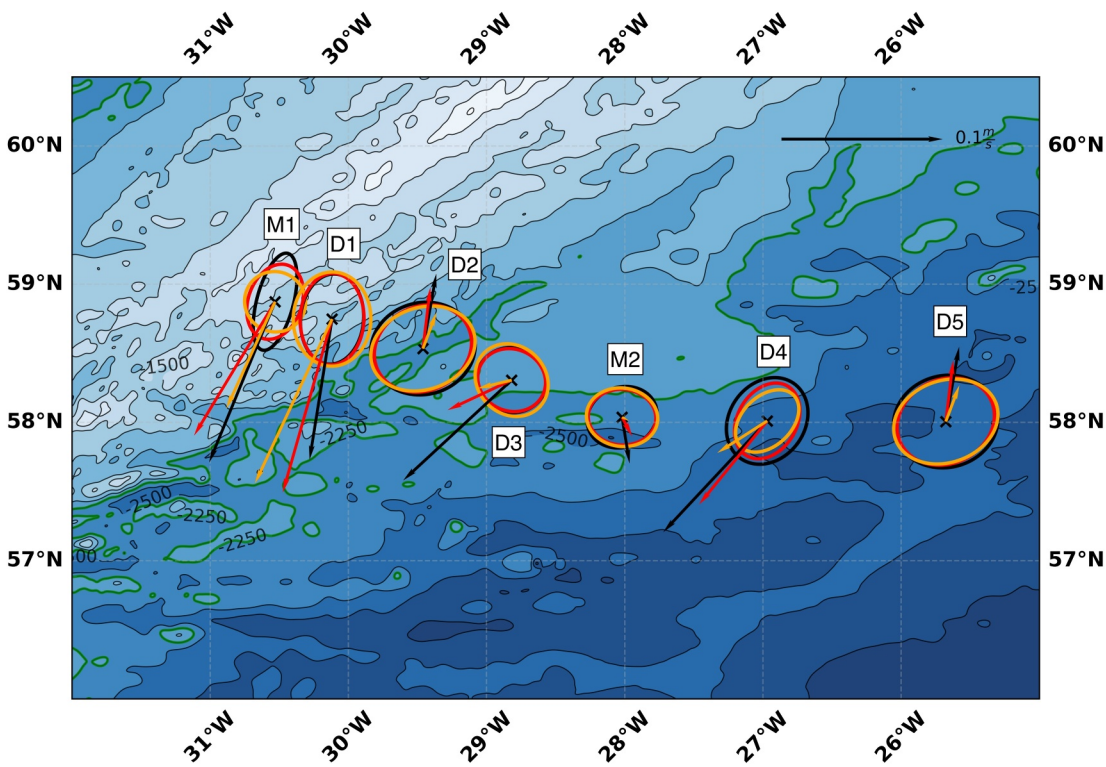

Figure 5. Variance ellipses (with axes scaled by variance) from the deepest three current meters at each mooring, Black, red, and orange correspond to the bottom, second from the bottom, and third from the bottom (respectively) instrument level at each mooring. Bottom instruments are 50 m above the bottom and the following two instruments are spaced approximately 250–300 m apart (vertical spacing varies at each mooring and readers can refer to Figure 2 for instrument configuration). Bathymetry contours are 250 m intervals and data is sourced from GEBCO data set. Green contour indicates 2,250 m contour for visual reference.

significant down slope component at the deepest level that decreases upwards. At D2 the near-bottom flow is strongly directional and aligned with the rift valley, while the mean flow at the two levels above shows a weak cross valley (eastward) component and similar counter-clockwise tilt of the variance ellipses. East of D2 the flow becomes more isotropic, which may indicate the stronger influence of barotropic effects from the strongly eddying upper ocean flow found in the Iceland Basin interior (Koman et al., 2020). The deep flow at D4 is an exception to this trend where a mean core of southward ISOW flow is present, leading to a notably stronger time-mean along slope component compared to the deep flow at M2. The more directional flow along the ridge suggests a strong localized topographic influence on ISOW flow at each mooring in addition to the large-scale topographic steering from the ridge slope.

3.3. Intra-Seasonal Variability

To further understand the intra-seasonal variability which appears to dominate the observations, we examine individual spectra at the current meters on selected moorings that are located within the cores of ISOW flow (D1, D2, D4, and D5). Variance preserving power spectra of along slope flow (the component used for transport calculations) show that each core of flow has unique temporal variability (Figure 6). At D1 the strongest variability is found at 10 and 14-day periods above the ISOW layer at 1,200 m (typically above 27.8 kg/m^3) and 1,500 m (typically within the ISOW layer). Elevated variability is also seen at ∼3-day periods and is also strongest at 1,200 m with decreasing magnitude with depth. The consistent decrease of variability magnitude with depth at all timescales is likely indicative of forcing by meandering or eddy variability in the overlying ERRC. In the deeper branches of ISOW flow, farther down the ridge slope and east of the dominant ERRC flow, the variability appears to be more intrinsic to the ISOW layer.

The strongest variability is found at D2 where bottom enhanced variability is seen at a broad range of intra-seasonal periods from 3 to 45 days. Maximum variability is seen in the 10–15-day period range but there are also notable peaks at 3–5-day periods, similar to D1. The weakest variability at D2 is found at depths above the rift valley walls but still within the ISOW layer (1,850- and 1,600-m instrument levels). This depth range is in the relatively quiescent intermediate layer between the upper ocean variability and the bottom enhanced valley flow. At D4, bottom enhanced flow is seen at all timescales but the along slope variability is generally weaker than at D1 and D2 and lacks the clear 10–15-day peak seen in flow along the ridge slope. Unlike ISOW cores at D1 and D2, the strongest variability is dominated by lower frequency variability in the 20–40-day period range. The northward flow at D5, in the western interior of the basin, is also dominated by lower frequency variability with maximum variability seen at 60-day periods. The shift in variability from higher to lower frequency indicates that the interior flow is dynamically distinct from the southward flowing ISOW cores. A similar distribution of variability is seen at Kanzow and Zenk (2014)'s array, where their easternmost mooring "W" was dominated by low-frequency variability, though generally weaker in magnitude compared to the OSNAP D5 mooring. This is likely due to the OSNAP line being farther south in the basin where surface eddy activity is stronger. The velocity spectra at the OSNAP moorings allow us to identify dynamically distinct regimes of the ISOW flow and highlight the clear spatial heterogeneity of the layer. Flow along the upper and middle ridge is dominated by high frequency variability and may be indicative of combined effects from rough topography, intrinsic plume variability, and upper ocean variability. Meanwhile, lower frequency upper ocean variability appears to dominate the interior flow (see further analysis in next section). These observations also show that a substantial change in spatial structure (branching of flow into multiple branches) and change in velocity variance occurs between the upstream arrays deployed by Kanzow and Zenk (2014) and Saunders (1996) and the OSNAP array. These changes appear to be largely linked to the increasingly rough and complex topography along the Reykjanes Ridge flank.

Kanzow and Zenk (2014) were able to attribute the dominant intra-seasonal variability to Topographic Rossby Waves (TRWs). While such waves may exist at the OSNAP line, the spectra and increased topographic roughness suggest they would likely be mired in a chaotic mix of other topographically forced processes. We can assess whether TRWs might be present by examining the high frequency cutoff of TRWs predicted from the dispersion relation (Pickart & Watts, 1990). Following (Johns & Watts, 1986), we can use a typical ISOW stratification $N \sim 10^{-3}$ s^{-1}, and mean ridge slope (ignoring the rough topography) $\alpha = 0.008$, to approximate a local high frequency cutoff of $\frac{2\pi}{\alpha N}$ ∼10 days. At D1, substantial variability is observed at shorter time scales, implying that TRWs may not be the dominant driver of variability here. Another way to test for the presence of TRWs is to examine the orientation of the variance ellipses in different frequency bands. If TRWs were present, the variance

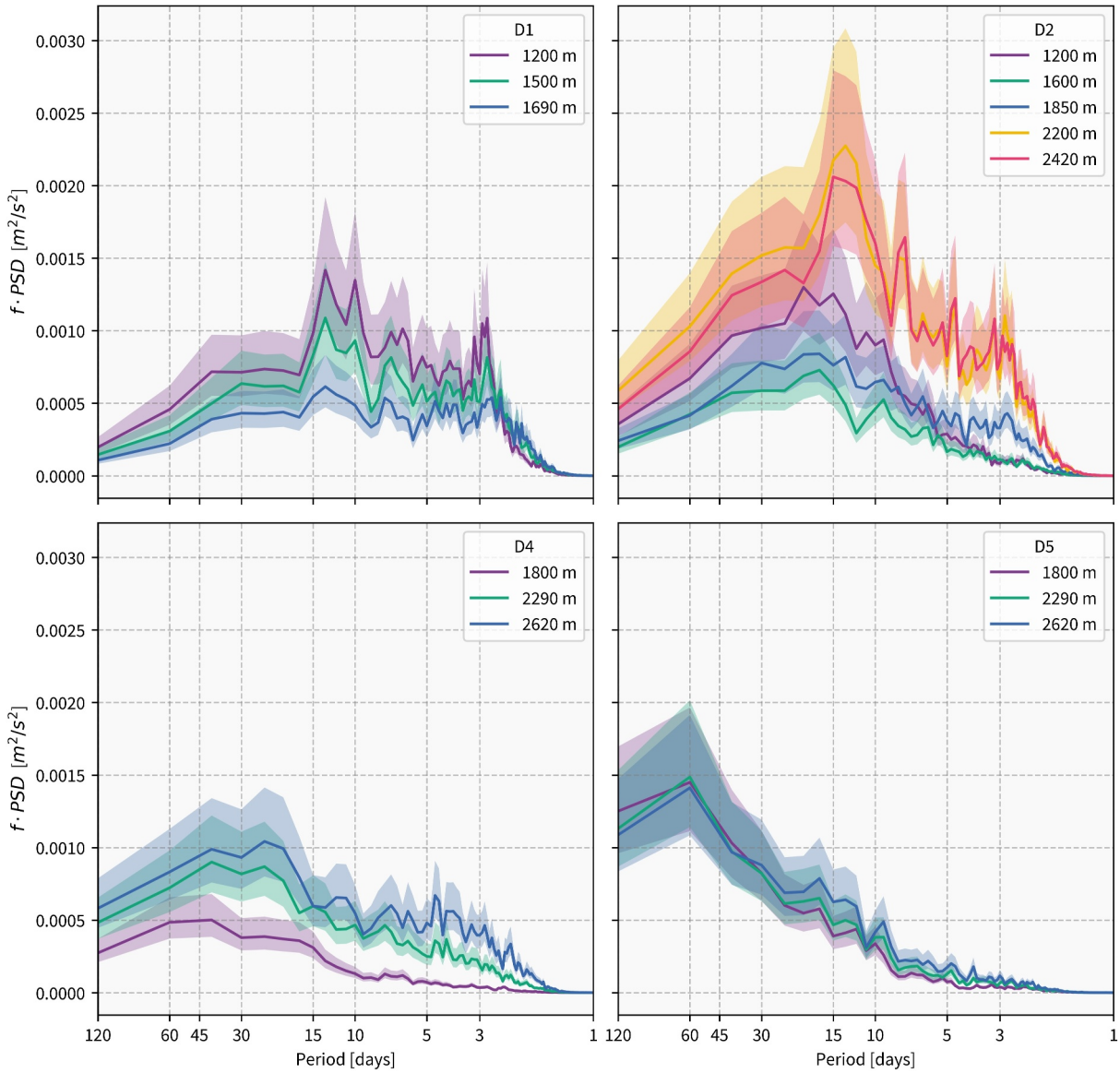

Figure 6. Variance preserving spectra for the along slope component of the flow measured by mooring current meters at moorings D1, D2, D4, and D5. The spectra are calculated using the 40-hr low-passed velocity records with the Welch method and half overlapping 120-day windows. Shading indicates 95% confidence levels.

ellipses associated with different period bands should rotate such that they are aligned across the isobaths in the high frequency limit. However, no such rotation was observed at any of the moorings along the upper ridge slope, and only a minimal signature of this is seen at mooring D4 at the base of the ridge (Supporting Information S1, Figure S1). TRWs would also tend to have a bottom intensified velocity structure which is only apparent at D2 where flow is trapped within a channel and likely has highly localized dynamics. Furthermore, the short wavelength topography along much of the ridge slope (~10–20 km) has scales on the same order as the predicted wavelengths of TRWs reported by Kanzow and Zenk (2014), suggesting that there would be substantial disruption of TRWs by the complex topography.

3.4. Barotropic Effects in ISOW-East

The variability of the deep ISOW branch is controlled by variability of both the southward flow at D4 and the predominantly northward flow at D5, which appears to partly recirculate the deep branch northward in the Iceland Basin interior (Johns et al., 2021). As shown in Figures 3 and 6 the flow variability at all deep levels on D5 is

nearly uniform in strength and nearly isotropic, suggesting that it may be forced by quasi-barotropic processes that are linked to the upper ocean variability in the Iceland Basin. From previous studies it is known that the surface eddy kinetic energy increases markedly toward the central Iceland Basin, driven by eddy and meandering activity associated with the North Atlantic Current (Böning et al., 2006; Foukal & Lozier, 2017; van Aken & Becker, 1996). We can use AVISO + ocean altimetry analysis to verify this by correlating altimetry derived surface velocities with the deep flows observed at the moorings. Mooring observed deep flows are daily averaged to match the resolution of the AVISO altimetry products for correlation. While the D5 mooring only monitors the flow below 1,800 m, geostrophic velocities estimated from altimetry correlate well ($r = 0.61$, $p < 0.05$) with the ISOW layer velocities measured here at the deepest instrument at D5). At D4, the correlation between deep velocities and surface geostrophic velocities is lower ($r = 0.28$, $p < 0.05$), because the ISOW flow at D4 likely contains a mix of intrinsic plume variability and local barotropic variability. By contrast, the ISOW flow between moorings M1 to M2 is not significantly correlated with surface geostrophic velocities estimated from altimetry. This result is slightly surprising for moorings M1 and D1 since it was expected that variability here may be coupled with upper ocean variability associated with the ERRC. Intra-seasonal variability at D1 is strongest at 1,200 m and decreases with depth at all timescales (Figure 6) suggesting the upper ocean is controlling flow variability in some manner. Flow here may still be coupled to the ERRC and upper ocean eddy variability but in a nonlinear relationship stemming from quasi-barotropic variability encountering the tallest ridge topography (Lavelle et al., 2012; Xie et al., 2022). Consequently ISOW-West transport is not correlated with the mean surface geostrophic velocities over that section while the ISOW-East transport is significantly correlated with the local surface velocities ($r = 0.55$, $p < 0.05$). This result highlights the strong effect of the ridge topography which appears to either limit or modify the influence of upper ocean variability on the net ISOW transport over ridge slope. In addition to the role of ridge topography, the lack of significant correlation between surface and deep velocities along the ridge slope may also be attributed to weakening barotropic variability due to distance from the North Atlantic Current. Eddy kinetic energy is known to decrease to the west of the Iceland Basin away from the highly energetic and variable North Atlantic Current (Foukal & Lozier, 2017). However, the magnitude of upper ocean variability driven by the North Atlantic Current and subpolar gyre variability is strong enough to imprint significant intraannual and interannual variations in the net ISOW transport when including the ISOW-East component of transport.

The large variability in overall ISOW transport also raises an interesting question of ISOW storage within the basin. Overflow transport at Faroe Bank Channel remains relatively steady and cannot account for the >5 Sv changes in transport. During periods of excess transport at the OSNAP line that are far above the mean, there must be either a balancing recirculation in the interior of the Iceland basin or a loss of volume of ISOW in the basin north of the OSNAP line. Conversely, during periods of very low or net northward transport measured by the array, there must be either a southward export of ISOW in the interior of the basin or net storage of ISOW north of the OSNAP line. Johns et al. (2021) found no evidence for net time-mean northward recirculation of ISOW in the interior of the Iceland Basin (east of mooring D5) but did not assess its variability. Given the large-amplitude eddy variability in the eastern Iceland Basin, it seems likely that large variations in ISOW layer transports could also occur there, however the degree to which they may compensate the observed ISOW transport variations in the OSNAP array remains uncertain.

3.5. EOF Decomposition

Next, we examine the along ridge flow over the upper and mid-ridge that is dominated by intra-annual variability and is the main contributor to the net ISOW transport. We apply an Empirical Orthogonal Function (EOF) (Preisendorfer & Mobley, 1988) decomposition to better understand the intrinsic variability of the flow along the flank of the Reykjanes Ridge. The along ridge component of flow at all current meters on moorings M1-M2 are used for the EOF decomposition with a 40-hr low pass filter applied to remove tidal influences. Moorings D4 and D5 are excluded because the large amplitude barotropic variability seen at these sites overshadows the variability along the upper and middle ridge. The resulting mode amplitudes from the EOF decomposition are gridded onto the same grid as the mooring observation grids used for transport calculations following Johns et al. (2021).

Only the first two modes of the EOF decomposition are significant when applying the North Test (North et al., 1982) and are the focus of the following analysis. Mode 1 explains 19% of the total velocity variance and is dominated by variability within the rift valley (Figure 7), coinciding with the location of the quasi-permanent branch of flow found within the valley. 14% of the velocity variance is explained by mode 2 which is

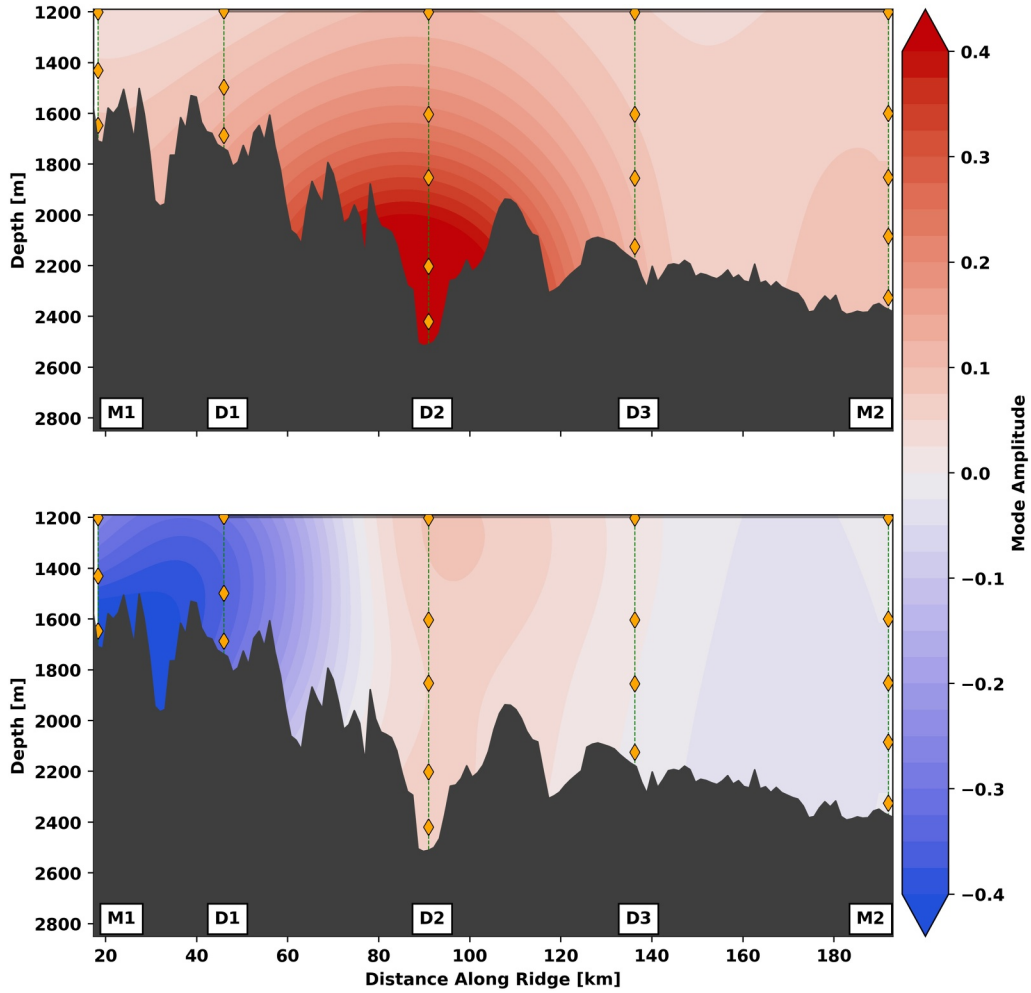

Figure 7. (a) EOF mode amplitude fields for the along slope component of observed flow for modes 1 (top- 19% velocity variance) and 2 (bottom-14% velocity variance). Mooring and instrument locations are indicated with dashed lines and orange diamonds, respectively. A 40 hr low pass filter is applied to the velocity records prior to the EOF decomposition to isolate subinertial variability.

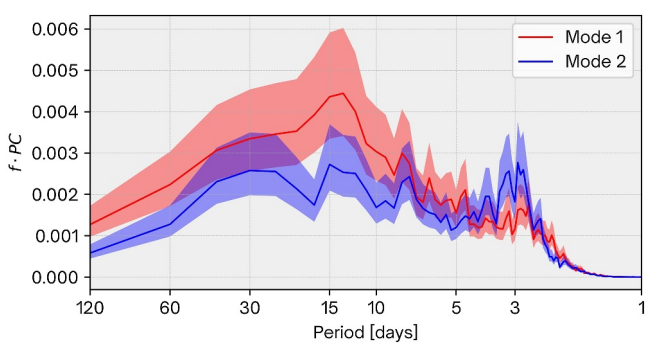

Figure 8. Variance preserving spectra for the principal components of modes 1 (red) and 2 (blue) from EOF decomposition. Spectra are calculated using 120 half overlapping windows with Welch's Method.

dominated by variance near the ridge crest where the westernmost branch of southward flow occurs. This mode has a banded structure with an opposite-signed anomaly over the D2 channel, which we believe is due to meandering of the western flow core over the upper ridge slope or also possibly linked to eddy or meandering activity in the overlying ERRC. The spectra of the first two principal components (Figure 8) shows that mode 1 has a strong peak near 10–15 days, similar to the bottom intensified peak in velocity spectra at mooring D2 (Figure 6) around which the respective maximum modal amplitude is centered. Mode 2 has several peaks, including ones near 10–15 days, 7 days, and 3 days that correspond to similar peaks in the D1 mooring spectra, and an additional lower-frequency peak near 20–25 days that is not clearly reflected in the D1 spectra.

The time varying velocity anomalies associated with each mode, reconstructed as the product of the principal components and mode amplitudes, can be used to estimate the transport anomaly along the ridge flank associated with each mode (Figure 9). Transport variance from modes 1 and 2 explain 75% and 5% of the total transport, respectively, despite explaining similar

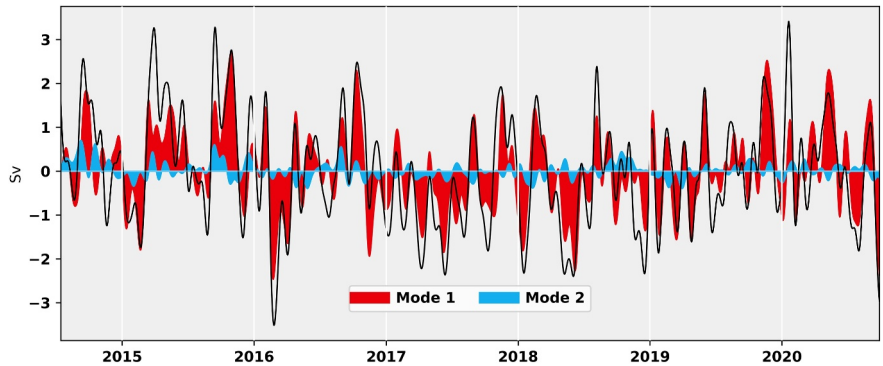

Figure 9. Transport anomaly (positive southwards) of ISOW from moorings M1-M2 and the reconstructed transport anomalies associated with modes 1 and 2. Mode transport anomaly is calculated using the gridded density fields and the velocity anomaly fields associated with each mode's principal component and modal amplitude.

amounts of velocity variance (19% and 14%). The bottom intensified rift valley flow is therefore dominating nearly all the transport variability in the along ridge ISOW flow as well as the intra-seasonal variability. The outsized influence of the first mode on transport variability is due to the distribution of amplitudes shown in Figure 9. The strongest variability of mode 1 is found within the rift valley and therefore always influencing transport variability while the mode 2 amplitudes at the edge of the ISOW layer implying that velocity variability associated with the mode is not always captured in the ISOW layer transport. Additionally, transport associated with mode 2 is much weaker than mode 1, which is due to the alternating amplitudes down the ridge flank that partially cancel each other in terms of net transport. The EOF decomposition shows that flow in the rift valley exerts a significant control on ISOW transport intra-annual variability. The principal component from mode 1 (and the flow and transport within the rift valley) show no significant correlation (or lagged correlation) with the thickness of the ISOW layer or in density within the valley. This suggests that flow strength is not linked to a shrinking or expanding of the ISOW layer.

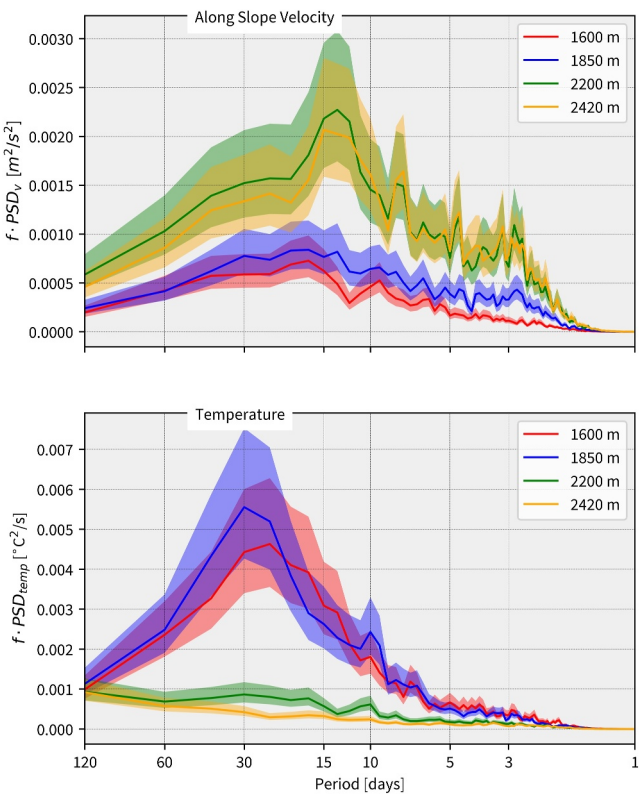

Figure 10. Along slope velocity (top) and temperature (bottom) variance preserving spectra at the D2 mooring's four deepest levels. Spectra are calculated using half overlapping 120 days windows with Welch's method. A 40 hr low pass filter is applied to isolate subinertial variability. Shading indicates 95% significance level.

The mechanism driving the bottom enhanced flow within the valley is not immediately clear. Our initial hypothesis was that these surges of bottom intensified flow might be related to spillage of anomalously dense waters (i.e., an overflow) into the rift valley from the upstream sill near 60ºN where the rift valley begins (Figure 1). Such a mechanism would lead to a relationship between velocity and density in the observations. However, velocity-potential density correlations at the bottom four instrument levels at D2 show no significant linear relationships. Furthermore, spectra of temperature and along slope velocity variability (Figure 10) show that elevated velocity variability does not correspond with temperature variability across numerous intra-seasonal frequencies. The spectra shows that while velocity variability is strongly bottom enhanced within the valley, temperature variability is stronger above the valley walls at 1,600 and 1,800 m, where variability is dominated by longer timescale variability (periods >30 days). The two deepest levels show much weaker temperature variability across all frequencies, despite dominating the velocity variability across all the current meter records. This clearly indicates that flow variability within the rift valley associated with mode 1 is not linked to hydrographic anomalies. Furthermore, cross spectral coherence between temperature and velocity is not significant at any intra-seasonal frequencies. If the flow is not linked to local changes in density (controlled primarily by temperature here), it may be that an along channel pressure gradient is present along the length of the rift valley.

However, our available data limits us from testing this idea, and further observations will likely be necessary to fully understand the mechanisms driving variability within the rift valley.

3.6. Geostrophy in the ISOW Layer

As the ISOW plume approaches the OSNAP line, it encounters increasingly rugged topography along the Reykjanes Ridge's eastern slope. Unlike the smoother Icelandic slope upstream of the OSNAP array, the topographic features along the ridge can reach horizontal scales comparable to the local Rossby radius of deformation (10's of km) and vertical scales on the same order of the ISOW layer thickness. So, while the ISOW layer is generally considered to be geostrophically balanced flow steered along the ridge slope, the geometry of the rift valley, as well as the generally increasing roughness of topography encountered along the ISOW path, raise the question of whether the ISOW flow maintains a geostrophic balance in this region of extremely rough topography. The co-located temperature, salinity, and velocity measurements allow for us to examine the cross ridge geostrophic shear and associated transport. Readers are referred to the Methods and Supporting Information S1 sections of this manuscript for the details on construction of the gridded fields used for geostrophic calculations.

The geostrophic velocity field is notably different than the observed velocity field, displaying only a singular branch of flow near the ridge crest (Figure 11a) and relatively weak geostrophic flow within the rift valley. The strongly bottom intensified core that is a quasi-steady feature of the current meter observations at moorings D2 and D3 (Figure 2a) is entirely absent. An estimate of the ageostrophic component of the along-ridge flow, obtained by differencing the geostrophic field from the directly measured flow field (Figure 11b), shows that the bottom enhanced ageostrophic signal extends well above the valley walls. Therefore, even though the geostrophic shear is not well constrained by our observations in bottom triangle regions, and particularly in the deep D2 channel, the ageostrophic flow at the D2 mooring extends up to depths where the observations should adequately resolve the geostrophic shear if it were present. In fact, the tilts of the deep isopycnals appear to be weakly reversed in the region of the D2 channel, as well as higher on the ridge slope (Figure 2b), which would imply decreasing geostrophic flow toward the bottom. This type of structure, where isopycnals plunge downward into the topography, has been linked to vigorous bottom-intensified mixing on slopes in both theoretical and observational studies (Garrett et al., 1993). Hydrographic sections with higher spatial resolution also consistently show downward tilting isopycnals such that the thermal wind shear weakens the southward geostrophic flow, and this structure is retained when we subsample CTD observations to match the mooring configuration (Figures S3 and S4 in Supporting Information S1).

The mean transport along the ridge flank below $\sigma_\theta = 27.8$ kg/m^3 estimated from direct current measurements is 4.2 Sv, while the geostrophic transport is substantially lower, at 2.9 Sv. The geostrophic estimate therefore recovers about ∼70% of the directly measured transport. Note that 4.2 differs slightly from the ISOW-East transport reported earlier. This is because taking gradients in hydrographic data on rectangular grids in the presence of slopes results in loss of coverage in the bottom grid cells, and to compare the two methods directly the transports are then summed over the same exact grid cells. Figure 12 shows that the largest divergence between the two transport estimates occurs in the region of the D2 valley and eastward to mooring D3, consistent with the velocity differences shown in Figure 11b.

To understand the influence of the bottom triangle regions on the transport calculation we can separate the transport into regions where lateral gradients are resolved (i.e., area in the plane of the mooring array not blocked laterally by topography or in a bottom triangle) and bottom triangle regions. Doing so shows that of the 4.2 Sv of the directly observed ISOW transport, 3.4 Sv arises from the well resolved region of the array while the remainder arises from the bottom triangle regions. The resolved region accounts for 2.5 Sv of geostrophic transport, meaning that 0.9 Sv of the total estimated ageostrophic transport (1.2 Sv) is contained within the resolved region of the array. This demonstrates that while uncertainty arises from bottom triangle filling methods, a significant portion of ageostrophic transport is obtained from above the bottom triangles where lateral gradients can be directly resolved by mooring observations.

The 30 days low passed time series of ageostrophic and geostrophic transports show that the low frequency components of transport are in close agreement but slightly offset, indicating that the geostrophic transport captures most of the low frequency (longer than 30 days) variability but misses a component of the mean transport (Figures 11c and 13). The unfiltered daily transports, with a standard deviation of 1.78 Sv, show that a portion of the high frequency variability is not captured by the geostrophic transport estimate (standard deviation of

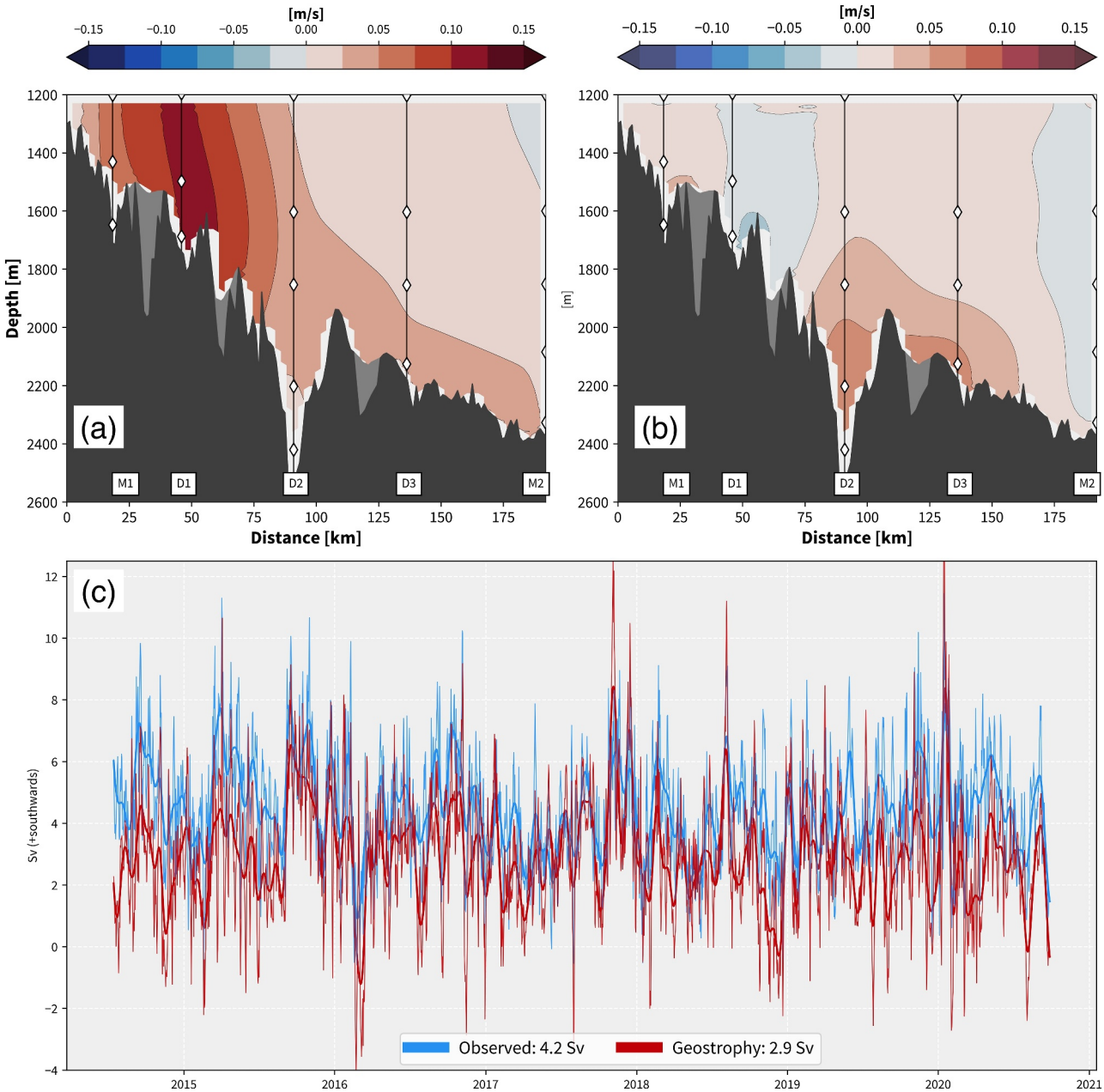

Figure 11. (a) Mean geostrophic velocities estimated from moored temperature and salinity measurements at moorings M1 to M2 (along the ridge slope). White diamonds indicate instrument locations (current meter and T/S recorders). (b) Mean difference between observed and geostrophic velocities form M1-M2. (c) Observed and geostrophic transport from 2014 to 2020. Bold lines show the 30 days low-passed daily time series and thin lines show unfiltered daily time series.

0.71 Sv). The ageostrophic component is > 3 Sv for roughly 30% the observational record and reaches extremes of 7 Sv. Figure 13 shows that the dominant timescales of the ageostrophic flow are between 10 and 20 days as well as at some higher frequency bands. This indicates that the geostrophic estimate of ISOW transport along the ridge flank misses both a key component of the mean transport and a portion of the intra-seasonal variability.

The valley flow also corresponds with the dominant mode of velocity variability and may be describing primarily ageostrophic variability. To understand if the mode variability and the ageostrophic transport are linked, we compute the geostrophic and ageostrophic transport isolated within the valley (from 80 to 110 km in cross-ridge distance shown in Figure 11). The geostrophic transport within the vicinity of the D2 valley is not significantly correlated with the Mode 1 principal component time series while the ageostrophic component of transport is

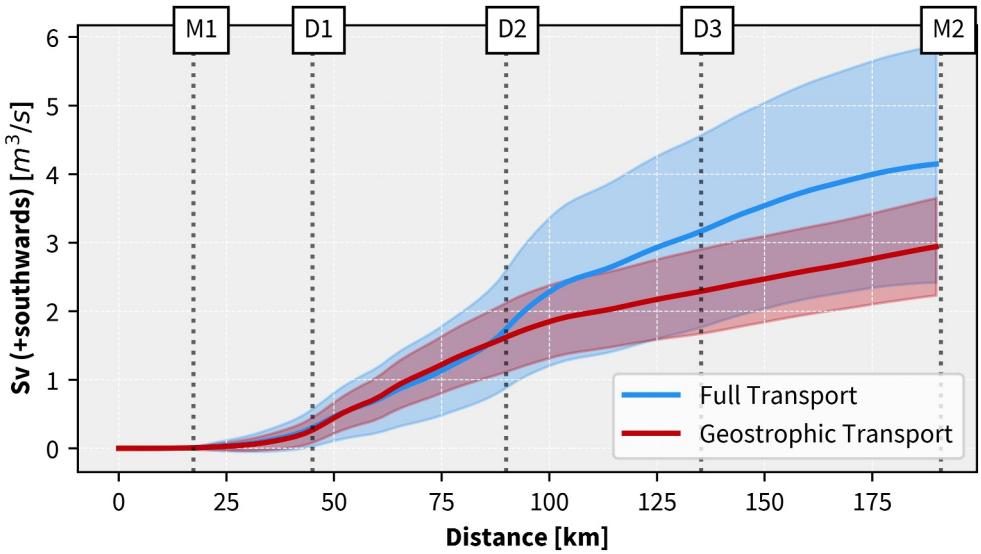

Figure 12. Cumulative observed (blue) and geostrophic (red) transport between moorings M1 to M2 along the Reykjanes Ridge slope (accumulated from west to east). Horizontal locations of moorings are indicated via vertical lines. Shading indicates ±1 standard deviation of daily transport time series with 40 hr low pass filter applied.

highly correlated with the Mode 1 principal component ($r = 0.8$, $p < 0.05$; Figures 14a and 14b). This shows that the leading mode of velocity variability, and the principal driver of along-slope transport variability, is in fact linked to the ageostrophic flow.

To better understand the strong ageostrophic flow, we utilize the principal component time series of Mode 1 from the EOF decomposition to generate composite profiles of velocity, temperature, salinity, and potential density during high and low Mode 1 periods (Figure 14c). Mooring data at the D2 mooring during peaks (troughs) above (below) one standard deviation of the principal component mean are averaged together to generate the high (low) composite profiles. Figure 14c shows the high and low composite velocity profiles split into the geostrophic and ageostrophic components. The ageostrophic *high* profiles show a clear bottom enhanced velocity with a maximum around 2,200 m that corresponds with overall mean flow in the valley. During *low* periods, the ageostrophic component is completely absent and even weakly negative (reversing flow in the valley). Meanwhile the geostrophic component is practically identical during *high* and *low* periods, further showing that the geostrophic flow and the first mode of velocity variability are not linked. What is slightly surprising is that there is no significant difference between the *high* and *low* period temperature, salinity, and potential density profiles (Figures 14d–14f). Thus, there appears to be no clear link between the ageostrophic flow maxima at 2,200 m and either density anomalies at the depth of the flow maximum or vertical density structure through the valley, in agreement with the analysis in the previous section.

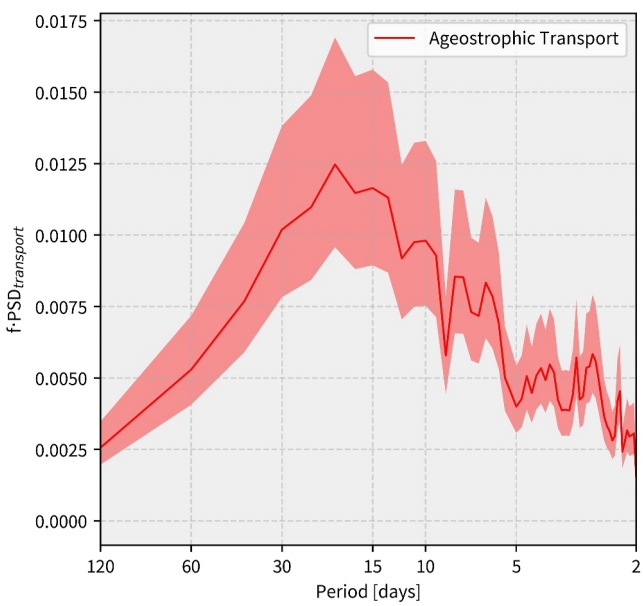

Figure 13. Ageostrophic transport variance preserving spectrum. Spectrum is calculated using half overlapping 120-day windows with Welch's method on the daily averaged ageostrophic transport time series. The ageostrophic component of velocity was calculated as the difference between the observed and geostrophically estimated velocity fields. The time evolving density fields were then used to calculate the net ageostrophic transport across the array. Shading indicates 95% confidence interval.

4. Impact of ISOW Transport Variability on the Subpolar AMOC

ISOW is an important component of the total AMOC in the subpolar gyre, responsible for roughly 1/3 of the total lower limb export across OSNAP (Johns et al., 2021). To understand how the time-varying ISOW flow may impact the AMOC strength, we compare the observed ISOW transport with the time-varying AMOC stream function derived from the full OSNAP-

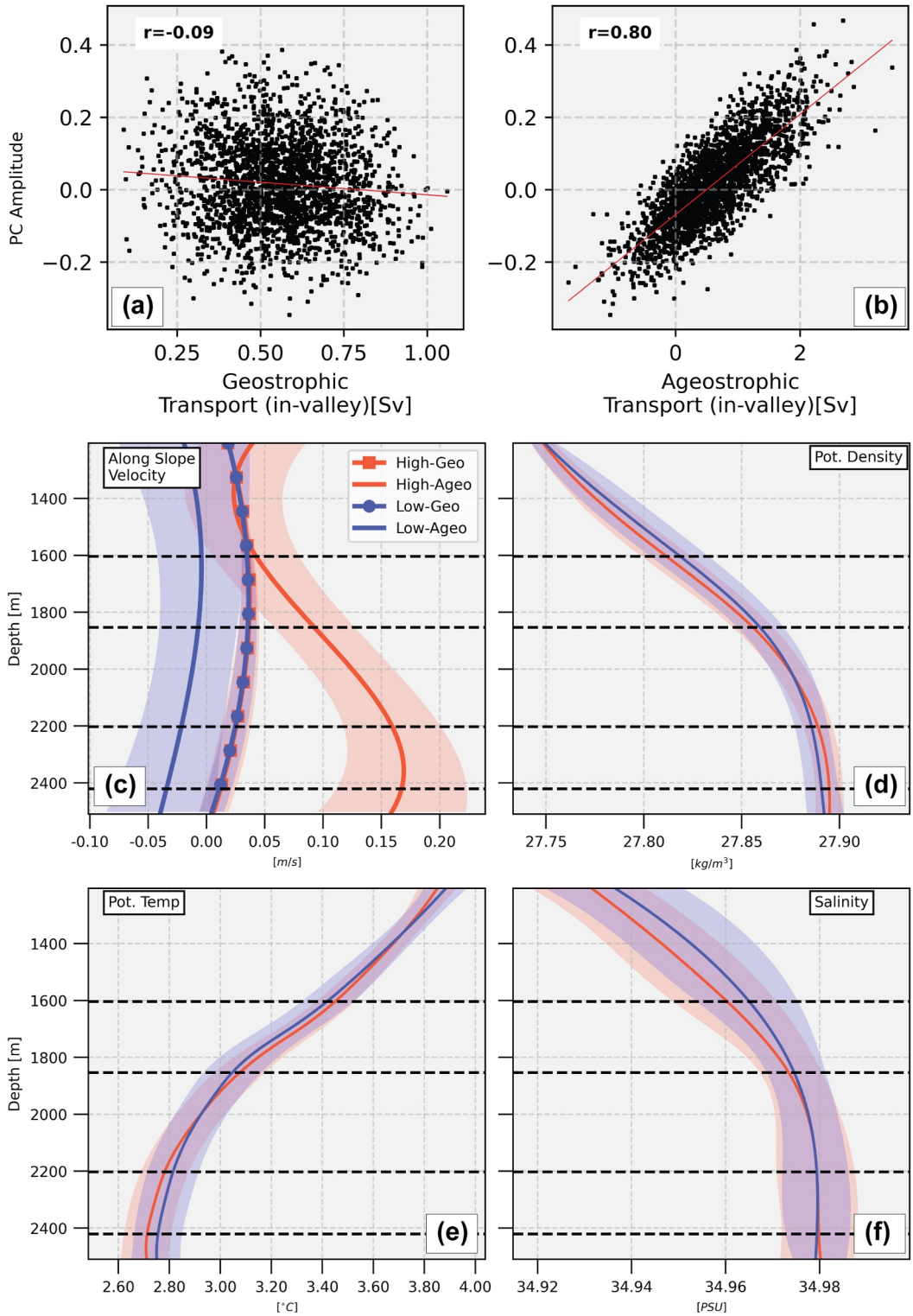

Figure 14. Correlations of geostrophic (a) and ageostrophic (b) transport within the rift valley with the Mode 1 principal component daily averaged time series. Mean composite profiles of along slope velocity (c) potential density (d), potential temperature (e), and salinity (f) at the D2 mooring within the rift valley during high (orange) and low (blue) events in the Mode 1 principal component time series. The profiles are generated by averaging profiles together peaks (troughs) above (below) 1 std. deviation from the principal component time series of the first mode. Panel (c) shows the velocity split into the geostrophic (lines with marker) and ageostrophic components (no markers). The shaded envelopes indicate ± one standard deviation from all profiles used to generate composites.

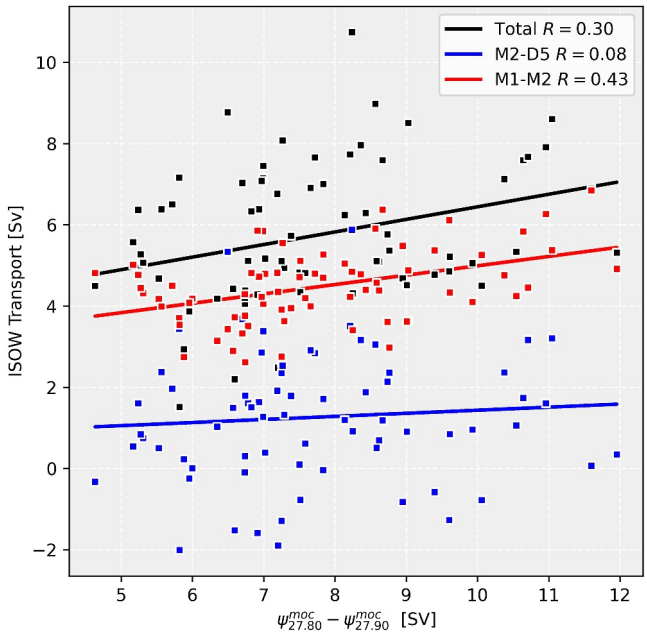

Figure 15. Comparison of monthly averaged ISOW transport (total, west, and east) with MOC stream function difference between the upper and lower bounds of ISOW density space (27.8–27.90 kg/m potential denity referenced to surface[3]). MOC and ISOW transport time series span 2014 July to 2020 July. R values for the total and M1-M2 are significant at $p \leq 0.05$. R values for M2-D5 are not significant.

EAST section that spans from Scotland to the East coast of Greenland. To isolate the portion of the stream function linked with waters in the ISOW density range, we take the difference of the stream function between $\sigma_\theta = 27.80$ and $\sigma_\theta = 27.90$. It is important to note that since the AMOC is calculated over the entire OSNAP-East section, Denmark Strait Overflow Water (DSOW) will also influence this density range. This density range encompasses the majority of the ISOW range while limiting influence of DSOW. However, since ISOW and DSOW do have overlapping density ranges, there is still some influence of the DSOW which would act to reduce the correlation between ISOW transport and OSNAP-East MOC strength in this density range.

The total ISOW transport is moderately correlated ($r = 0.27$, $p < 0.01$) with the AMOC strength in this density range. Interestingly, nearly all the correlation is due to the ISOW-West flow along the ridge slope ($r = 0.37$, $p < 0.01$) while the interior ISOW-East flow is not significantly correlated ($r = 0.07$) with the MOC streamfunction in the deep layers that encompass ISOW and DSOW (Figure 15). If this calculation is repeated without the lower bound of 27.90 to include all waters denser than 27.80, the results show no significant change. The ISOW-East flow, which drives extensive ISOW variability across the OSNAP moorings in the Iceland Basin, has only a minimal impact on the deep MOC strength across the entire OSNAP-East line. This further supports the presence of a deep circulation within the Iceland Basin that stores and releases ISOW but does not affect the net overturning. The net export of Lower North Atlantic Deep Water across the OSNAP line instead appears to be most directly impacted by the varying ISOW transport along the upper and mid-Reykjanes Ridge slope, which in turn is affected by ageostrophic processes associated with the rough topography of the Reykjanes Ridge.

5. Discussion

The results presented here demonstrate significant spatial and intra-seasonal variability of ISOW transport in the Iceland Basin at the OSNAP mooring array and show that ageostrophic flow is significant to the net export into the North Atlantic. The findings have immediate implications for the current understanding of ISOW circulation in the Iceland Basin, the deep export pathways into the larger Atlantic circulation, and for areas of attention in future modeling efforts surrounding the overflow layer.

ISOW flow along the Reykjanes Ridge slope is likely governed by a combination of topographic interactions, meso- and submesoscale instabilities, and other non-linear dynamics. The results presented here clearly show that the non-geostrophic dynamics are responsible for a significant portion of the mean ISOW transport and AMOC lower layer export across OSNAP-East, as well as driving substantial intra-seasonal variability. High resolution modeling work by Corre et al. (2020) also suggests that non-linear dynamics and bottom drag curl from the ridge topography play a significant role in the dynamical balance on a gyre scale. Numerous recent studies have also highlighted the importance of mesoscale, submesoscale, and small-scale processes in controlling deep water mass transformations on a large scale (Callies, 2018; Ferrari et al., 2016; Wenegrat et al., 2018). These results should motivate further investigations into the smaller scale processes as they are clearly impacting the larger scale ISOW export and likely play an important role in setting the water properties that are exported into Lower North Atlantic Deep Water.

The magnitude of the ageostrophic transport is a surprising result, especially in the context of ISOW as a deep western boundary current thought be geostrophic and steered by topography. Furthermore, the lack of a clear link between local flow and density changes in the D2 valley, where ageostrophic flow is strongest, leaves few clues as to the processes that may be driving the flow. Given the underestimate of the ISOW mean flow by geostrophy near moorings D2 and D3 (Figure 11), we look to other terms in the Navier-Stokes equations that may possibly be important in the cross-slope momentum balance, particularly the turbulent stress $\left(\frac{d\langle u'u'\rangle}{dx}, \frac{d\langle u'v'\rangle}{dy}\right)$ and non-linear

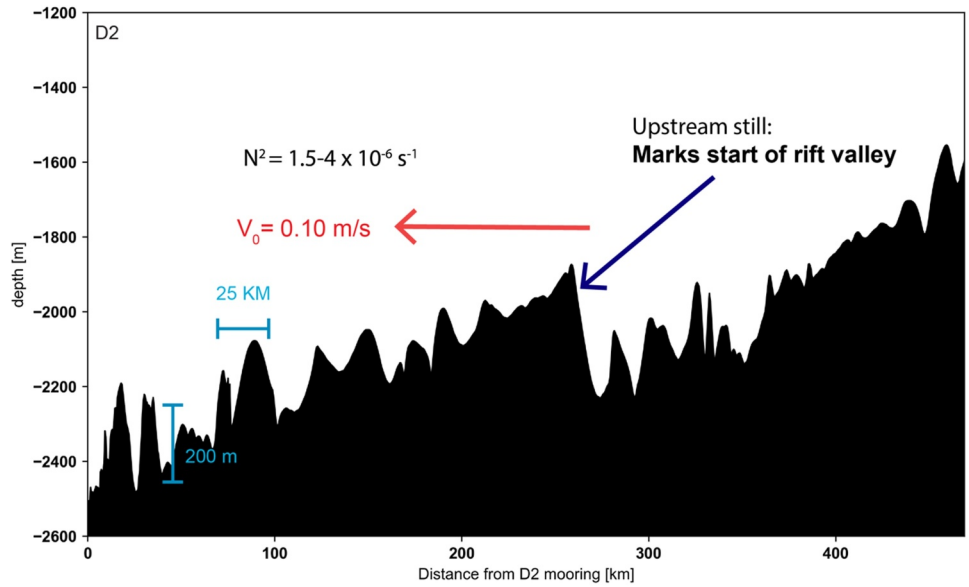

Figure 16. Topography transects starting at D2 Mooring extending 450 km upstream along the Reykjanes Ridge slope. Key vertical and horizontal scales, mean flow, and stratification are indicated. Bathymetry is derived from the GEBCO 2019 Global Ocean Atlas. Upstream sill that marks the beginning of the rift valley is indicated. Distances are positive northwards away from the D2 mooring.

terms $\left(u\frac{du}{dx}, v\frac{du}{dy}\right)$. Here, u and v refer to mean cross and along components of low while u' and v' are the perturbation quantities. Since there is only a single mooring within the valley and no up or downstream information accompanying the mooring observations, robust quantitative estimates of these terms are difficult. However, scaling analysis can provide some insight into the likely magnitude of these terms.

Using mooring records to estimate typical mean flow u and v, and perturbations u' and v' (both of order 0.1 m/s), we find that even at relatively small (dx, dy) scales of 10 km, upper bound estimates for both the turbulent stress and non-linear terms are at least an order of magnitude less than the momentum imbalance between the pressure gradient and the observed along-slope flow. Either the valley would need to be considerably narrower (smaller dx) or the velocity anomalies much larger for these terms to clearly balance the momentum deficit. Froude number estimates of the valley flow are also well below critical values suggesting that flow is not in the immediate vicinity of an overflow into the valley (or some other critical flow generated by topography), although it may be possible that multiple upstream spillages into the valley may evolve into that state observed at D2. Hydraulic control at over particularly prominent upstream sills may also play a role in the channel flow (Hogg, 1983), although the rough topography makes it difficult to discern any exact sill location. Further observations are needed within the valley to truly decipher the processes that govern the ageostrophic flow here.

While further observations are needed within the rift valley to understand the processes leading to ageostrophic flow, the range of processes that could contribute to ageostrophic flow can be assessed in terms of key parameters of the flow, following Klymak (2018). This framework separates flow into linear or non-linear flow states and the topographic roughness into either small or large scale regimes, leading to 4 possible combinations of flow states. Following this framework, the expected flow regime depends on two key parameters: Nh/U and Uk/f where N = mean stratification, U = mean flow, h = topographic height, k = horizontal topographic wavelength, and f = coriolis parameter (Klymak (2018; their Figure 1). Mean flow speeds in the cores are typically 10–15 cm/s and ambient stratification N is on the order of 1.5–4 $\times$ 10^{-6} s^{-1}, and a section of the topography along the ridge upstream from D2 shows numerous 10–20 km scale features with 100–300-m vertical extents (Figure 16). Based on these parameters and the highly variable strength of ISOW flow within the rift valley (0.05 to greater than 0.2 m/s) we can expect non-linear flows and small scale topographic regimes, resulting in a combination of trapped, radiated, and breaking internal waves.

Furthermore, Figure 16 shows the sill marking the start of the rift valley as a prominent topographic feature where ISOW may spill into the valley. However, the upstream sill may not be the sole location for ISOW to descend into the valley and instead it may descend into the valley anywhere along the valley as sporadic cascades of flow from higher along the ridge slope. This may explain the consistently well-mixed water column within the valley and flow variability that does not correlate with either surface velocities or velocities beyond the immediate vicinity of the D2 channel. D3 is the only mooring that shows any significant correlation with D2, which suggests that flow at D3 may be linked to the processes driving both the mean flow and variability within the rift valley.

Farther south along the Mid-Atlantic Ridge near the Azores, an extensive examination of rift valley flow conducted by Lahaye et al. (2019) provides useful insight into the results shown here. Through observational and numerical model methods, they found the mean flow to be driven by a combination of overlying mesoscale variability and tidal rectification. The Reykjanes Ridge hosts an active internal tide field (Vic et al., 2020) and high upper ocean eddy activity, implying that Lahaye et al. (2019)'s conclusions may also describe the governing dynamics of the rift valley flow at the OSNAP line. Additionally, the rift valley extends over 200 km upstream and may be large enough to generate an along channel pressure gradient rather than a cross slope thermal wind gradient. Essentially a north-south pressure gradient would not be able to geostrophically adjust because of the narrow zonal width of the valley and instead drive flow along the direction of the gradient. Upstream measurements of inflow into the valley and the upstream pressure would be required to thoroughly assess the presence of an along channel type flow. A further complication is that the topographic ssresponses predicted from the scale analysis in the previous paragraph would likely mask a clear signal from an along channel pressure gradient. Interestingly, (Lahaye et al., 2019 's model simulations also failed to generate the well mixed water column found in rift valley observations, suggesting that non-linear and small-scale processes unresolved by the model may be a key component of the flow within rift valleys. The presence of high frequency (3-day and shorter periods) variability at D2 (and D1 and D4) supports the presence of instabilities within the deep flow, possibly due to baroclinic instability or some sort of topographically driven instabilities such as flow blocking, internal tide or lee wave breaking (Klymak, 2018; Klymak et al., 2021).

The weak influence of basin interior variability on net ISOW export and the deep layers ($\geq$27.8 kg/m^3) of the MOC across OSNAP-East suggests the presence of variable recirculation within the Iceland Basin that may have capacity to store/release ISOW for export into Lower North Atlantic Deep Water. The lack of correlation between ISOW-East transport in the Iceland Basin and deep MOC transport across the entire OSNAP-East section indicates ISOW-East variability may be related to basin interior flow that does not cross the Reykjanes Ridge and may be locally compensated via recirculation. The spreading of bottom salinity signals from west to east across the Iceland Basin shown by Devana et al. (2021) further support the presence of recirculating abyssal waters and highlight how the interior Iceland Basin water properties evolve in response to the recirculating flow by having a delayed response (relative to the boundary) to a major salinity change. Recent results by Castrillejo et al. (2022), as well as several other previous studies referenced therein, have suggested a direct pathway of ISOW through the interior of the basin but the results shown here raise doubts about such a pathway. Model simulations suggest that anticyclonic recirculation cells are present and linked with surface flows (Xu et al., 2018). Johns et al. (2021) estimated ~0.7 Sv of possible recirculation east of mooring D5 across to the Hatton Bank and cumulative transport estimates (not shown here) across the ISOW layer using the OSNAP-wide gridded product (Fu et al. (2023a)) show similar estimates. However, observations within the Iceland basin are sparse and consequently the OSNAP basin-wide analysis is unlikely to fully resolve the details of the both the zonal and meridional Iceland Basin interior flow structure.

The strong variability of east of the ridge slope may have minimal effect on the MOC but could directly influence the spreading pathways of ISOW on the eastern side of the Mid- Atlantic Ridge. Understanding the interior circulation can provide better understanding of the timescales on which ISOW is stored and released from the basin and how that circulation modulates export pathways. Additionally, a key unanswered question that stems from these results is whether the increased flow observed at D4 in recent years follows the more westerly flow through gaps in the ridge, stays on the eastern flank of the ridge for southward export, or is deflected into interior recirculation. To understand how this partitioning occurs, a clearer understanding of the interior circulation combined with the variability described here is necessary.

More broadly, the spatial heterogeneity of the ISOW flow and clear presence of significant ageostrophic/nonlinear flow should prompt extra scrutiny of modeled ISOW flows when examining both ISOW export

pathways and the lower limb of the MOC in the subpolar gyre. Treating ISOW as a predominantly deep western boundary flow and assessing its variability as a single bulk quantity may be a somewhat misleading metric for model validations. In the modeling results from Xu et al. (2018) that show weaker and less variable ISOW export across the OSNAP line, the area of the rift valley shows weakly northward rather than a strongly southward branch of flow and only shows a singular branch of southward flow along the ridge flank located between moorings D1 and D2. Zou et al. (2017, 2020) show simulated ISOW flows that also fail to resolve the deep rift valley flow with only a singular branch of flow west of D2. Interestingly, both simulated ISOW flows bear more resemblance to the geostrophic structure shown here, suggesting that the simulated ISOW flows may adequately generate only the geostrophic component of ISOW export. The dominant variability from ageostrophic components demonstrated here may be underrepresented in the simulations. Additionally, recent work by Zhai et al. (2021) examining the spreading of ISOW (and other LNADW components) using ECCOv4 reanalysis output may also have an unrealistic structure, and consequently variability, given that they estimate only 0.6 Sv of ISOW export from the Iceland Basin. While the authors do not show the ISOW velocity structure, such a departure from the observed transport (5.3–5.8 Sv) suggests that ISOW transport (and the associated variability) is not adequately resolved. Consequently, the conclusions drawn from simulations of ISOW flow that lack key components of variability may not fully account for the spatial and temporal distribution of ISOW that is available for export. A useful guidance for future studies may be to compare mean flow and variability of simulated ISOW at each of the main velocity cores, rather than a single bulk comparison that may inadvertently mask important details. This idea builds on the conclusions of Lozier et al. (2022) that much of the ISOW exported into the North Atlantic may not be driven by the classical definition of deep western boundary currents but rather a more geographically diffuse set of interior and boundary flows. The results shown here suggest that ageostrophic and non-linear, and meso- to submeso- scale dynamics may control some of these flows and can leave significant imprints on the large-scale circulation in the lower limbs of the subpolar gyre.

Data Availability Statement

Mooring and cruise data from the OSNAP project used in this research are sourced from Fu, Lozier, Biló, et al. (2023). Data used in this study is available at Fu, Lozier, Carrilho Biló, et al. (2023).

Acknowledgments
The authors would like to thank the crews and captains of the R/V Armstrong, as well as the University of Miami Ocean Technology Group for their assistance the seagoing operations supporting this research. Financial support for this research was provided by the US National Science Foundation under Grants OCE-1259398 and OCE-1756231. We would also like to thank Alberto Garabato, Eleanor Frajka-Williams, Mohamed Iskandarani, and Tamay Ozgokomen for their useful insight and discussions.

References

Aken, H. M. V., & Becker, G. (1996). Hydrography and through-flow in the North-Eastern North Atlantic Ocean: The NANSEN project. *Progress in Oceanography*, *38*(4), 297–346. https://doi.org/10.1016/s0079-6611(97)00005-0

Beaird, N., Rhines, P., & Eriksen, C. C. (2013). Overflow waters at the Iceland–Faroe ridge observed in multiyear seaglider surveys. *Journal of Physical Oceanography*, *43*(11), 2334–2351. https://doi.org/10.1175/jpo-d-13-029.1

Böning, C. W., Scheinert, M., Dengg, J., Biastoch, A., & Funk, A. (2006). Decadal variability of subpolar gyre transport and its reverberation in the North Atlantic overturning. *Geophysical Research Letters*, *33*(21), L21S01. https://doi.org/10.1029/2006gl026906

Bower, A. S., Lozier, M. S., Gary, S. F., & Böning, C. W. (2009). Interior pathways of the North Atlantic meridional overturning circulation. *Nature*, *459*(7244), 243–247. https://doi.org/10.1038/nature07979

Callies, J. (2018). Restratification of abyssal mixing layers by submesoscale baroclinic eddies. *Journal of Physical Oceanography*, *48*(9), 1995–2010. https://doi.org/10.1175/jpo-d-18-0082.1

Castrillejo, M., Casacuberta, N., Vockenhuber, C., & Lherminier, P. (2022). Rapidly increasing Artificial Iodine highlights pathways of Iceland-Scotland overflow water and Labrador Sea water. *Frontiers in Marine Science*, *9*. https://doi.org/10.3389/fmars.2022.897729

Corre, M. L., Gula, J., & Tréguier, A.-M. (2020). Barotropic vorticity balance of the North Atlantic subpolar gyre in an eddy-resolving model. *Ocean Science*, *16*(2), 451–468. https://doi.org/10.5194/os-16-451-2020

Devana, M. S., Johns, W. E., Houk, A., & Zou, S. (2021). Rapid freshening of Iceland Scotland overflow water driven by entrainment of a major upper ocean salinity anomaly. *Geophysical Research Letters*, *48*(22), e2021GL094396. https://doi.org/10.1029/2021GL094396

Ferrari, R., Mashayek, A., McDougall, T. J., Nikurashin, M., & Campin, J.-M. (2016). Turning ocean mixing upside down. *Journal of Physical Oceanography*, *46*(7), 2239–2261. https://doi.org/10.1175/JPO-D-15-0244.1

Foukal, N. P., & Lozier, M. S. (2017). Assessing variability in the size and strength of the North Atlantic subpolar gyre: North Atlantic subpolar gyre variability. *Journal of Geophysical Research: Oceans*, *122*(8), 6295–6308. https://doi.org/10.1002/2017jc012798

Fu, Y., Lozier, M. S., Biló, T. C., Bower, A. S., Cunningham, S. A., Cyr, F., et al. (2023a). Seasonality of the meridional overturning circulation in the subpolar North Atlantic. *Commun Earth Environ*, *4*(1), 181. https://doi.org/10.1038/s43247-023-00848-9

Fu, Y., Lozier, M. S., Carrilho Biló, T., Bower, A., Cunningham, S., Cyr, F., et al. (2023b). Meridional overturning circulation observed by the overturning in the subpolar north Atlantic program (OSNAP) Array from August 2014 to June 2020 [Dataset]. *Georgia Institute of Technology*. https://doi.org/10.35090/GATECH/70342

Ganachaud, A. (2003). Error budget of inverse box models: The North Atlantic. *Journal of Atmospheric and Oceanic Technology*, *20*(11), 1641–1655. https://doi.org/10.1175/1520-0426(2003)020<1641:EBOIBM>2.0.CO;2

Garrett, C., MacCready, P., & Rhines, P. (1993). Boundary mixing and arrested Ekman layers: Rotating stratified flow near a sloping boundary. *Annual Review of Fluid Mechanics*, *25*(1), 291–323. https://doi.org/10.1146/annurev.fl.25.010193.001451

GEBCO Compilation Group. (2023). GEBCO 2023 grid. Distributed by OpenTopography. [Dataset of global bathymetry]. *GEBCO*. https://doi.org/10.5069/G9D21VTT

Hansen, B., Larsen, K. M. H., Hátún, H., & Østerhus, S. (2016). A stable Faroe Bank Channel overflow 1995–2015. *Ocean Science*, *12*(6), 1205–1220. https://doi.org/10.5194/os-12-1205-2016

Hansen, B., & Østerhus, S. (2000). North Atlantic–Nordic Seas exchanges. *Progress in Oceanography*, *45*(2), 109–208. https://doi.org/10.1016/s0079-6611(99)00052-x

Hansen, B., & Østerhus, S. (2007). Faroe bank channel overflow 1995–2005. *Progress in Oceanography*, *75*(4), 817–856. https://doi.org/10.1016/j.pocean.2007.09.004

Hogg, N. G. (1983). Hydraulie control and flow separation in a multi-layered fluid with applications to the Vema Channel. *Journal of Physical Oceanography*, *13*(4), 695–708. https://doi.org/10.1175/1520-0485(1983)013<0695:HCAFSI>2.0.CO;2

Johns, W., Devana, M., Zou, S., & Houk, A. (2021). Moored observations of the Iceland-Scotland Overflow plume along the eastern flank of the Reykjanes Ridge. *Journal of Geophysical Research: Oceans*, *126*(8),e2021JC017524. https://doi.org/10.1029/2021jc017524

Johns, W. E., & Watts, D. R. (1986). Time scales and structure of topographic Rossby waves and meanders in the deep Gulf Stream. *Journal of Marine Research*, *44*(2), 267–290. https://doi.org/10.1357/002224086788405356

Kanzow, T., & Zenk, W. (2014). Structure and transport of the Iceland Scotland Overflow plume along the Reykjanes Ridge in the Iceland Basin. *Deep Sea Research Part I: Oceanographic Research Papers*, *86*, 82–93. https://doi.org/10.1016/j.dsr.2013.11.003

Klymak, J. M. (2018). Nonpropagating form drag and turbulence due to stratified flow over large-scale abyssal hill topography. *Journal of Physical Oceanography*, *48*(10), 2383–2395. https://doi.org/10.1175/JPO-D-17-0225.1

Klymak, J. M., Balwada, D., Garabato, A. N., & Abernathey, R. (2021). Parameterizing nonpropagating form drag over rough bathymetry. *Journal of Physical Oceanography*, *51*(5), 1489–1501. https://doi.org/10.1175/JPO-D-20-0112.1

Koman, G., Johns, W. E., & Houk, A. (2020). Transport and evolution of the East Reykjanes Ridge Current. *Journal of Geophysical Research: Oceans*, *125*(10). https://doi.org/10.1029/2020JC016377

Koman, G., Johns, W. E., Houk, A., Houpert, L., & Li, F. (2022). Circulation and overturning in the eastern North Atlantic subpolar gyre. *Progress in Oceanography*, *208*, 102884. https://doi.org/10.1016/j.pocean.2022.102884

Lahaye, N., Gula, J., Thurnherr, A. M., Reverdin, G., Bouruet-Aubertot, P., & Roullet, G. (2019). Deep currents in the Rift Valley of the North Mid-Atlantic Ridge. *Frontiers in Marine Science*, *6*. https://doi.org/10.3389/fmars.2019.00597

Lake, I., & Lundberg, P. (2006). Seasonal barotropic modulation of the deep-water overflow through the Faroe bank channel. *Journal of Physical Oceanography*, *36*(12), 2328–2339. https://doi.org/10.1175/jpo2965.1

Lavelle, J. W., Thurnherr, A. M., Mullineaux, L. S., McGillicuddy, D., & Ledwell, J. R. (2012). The prediction, verification, and significance of Flank Jets at mid-ocean ridges. *Oceanography*, *25*(1), 277–283. https://doi.org/10.5670/oceanog.2012.26

Lozier, S., Bower, A. S., Furey, H. H., Drouin, K. L., Xu, X., & Zou, S. (2022). Overflow water pathways in the North Atlantic. *Progress in Oceanography*, *208*, 102874. https://doi.org/10.1016/j.pocean.2022.102874

Lozier, S., Li, F., Bacon, S., Bahr, F., Bower, A. S., Cunningham, S. A., et al. (2019). A sea change in our view of overturning in the subpolar North Atlantic. *Science*, *363*(6426), 516–521. https://doi.org/10.1126/science.aau6592

North, G. R., Bell, T. L., Cahalan, R. F., & Moeng, F. J. (1982). Sampling errors in the estimation of empirical orthogonal functions. *Monthly Weather Review*, *110*(7), 699–706. https://doi.org/10.1175/1520-0493(1982)110<0699:SEITEO>2.0.CO;2

Petit, T., Lozier, S., Josey, S. A., & Cunningham, S. A. (2020). Atlantic deep water formation occurs primarily in the Iceland Basin and Irminger Sea by local buoyancy forcing. *Geophysical Research Letters*, *47*(22). https://doi.org/10.1029/2020GL091028

Pickart, R. S., & Watts, D. R. (1990). Deep western boundary current variability at cape Hatteras. *Journal of Marine Research*, *48*(4), 765–791. https://doi.org/10.1357/002224090784988674

Preisendorfer, R. W., & Mobley, C. D. (1988). *Principal component analysis in meteorology and oceanography*. Elsevier ; Distributors for the U. S. and Canada, Elsevier Science Pub. Co.

Saunders, P. M. (1996). The flux of dense cold overflow water southeast of Iceland. *Journal of Physical Oceanography*, *26*(1), 85–95. https://doi.org/10.1175/1520-0485(1996)026<0085:TFODCO>2.0.CO;2

Vic, C., Ferron, B., Thierry, V., Mercier, H., & Lherminier, P. (2020). Tidal and near-inertial internal waves over the Reykjanes Ridge. *Journal of Physical Oceanography*, *51*(2), 419–437. https://doi.org/10.1175/jpo-d-20-0097.1

Wenegrat, J. O., Callies, J., & Thomas, L. N. (2018). Submesoscale baroclinic instability in the bottom boundary layer. *Journal of Physical Oceanography*, *48*(11), 2571–2592. https://doi.org/10.1175/JPO-D-17-0264.1

Xie, X., Wang, Y., Liu, X., Wang, J., Xu, D., Liu, T., et al. (2022). Enhanced near-bottom circulation and mixing driven by the surface eddies over abyssal seamounts. *Progress in Oceanography*, *208*, 102896. https://doi.org/10.1016/j.pocean.2022.102896

Xu, X., Rhines, P. B., & Chassignet, E. P. (2018). On mapping the diapycnal water mass transformation of the Upper North Atlantic Ocean. *Journal of Physical Oceanography*, *48*(10), 2233–2258. https://doi.org/10.1175/jpo-d-17-0223.1

Zhai, Y., Yang, J., Wan, X., & Zou, S. (2021). The eastern Atlantic basin pathway for the export of the North Atlantic deep waters. *Geophysical Research Letters*, *48*(24), e2021GL095615. https://doi.org/10.1029/2021GL095615

Zou, S., Lozier, S., Zenk, W., Bower, A., & Johns, W. (2017). Observed and modeled pathways of the Iceland Scotland Overflow Water in the eastern North Atlantic. *Progress in Oceanography*, *159*, 211–222. https://doi.org/10.1016/j.pocean.2017.10.003